



HAL
open science

A novel hydraulic bulge test in hot forming conditions

A. Boyer, N. Demazel, J. Coër, Muriel Carin, H. Laurent, M.C. Oliveira

► To cite this version:

A. Boyer, N. Demazel, J. Coër, Muriel Carin, H. Laurent, et al.. A novel hydraulic bulge test in hot forming conditions. *Journal of Materials Processing Technology*, 2023, 316, pp.117917. 10.1016/j.jmatprotec.2023.117917 . hal-04649909

HAL Id: hal-04649909

<https://hal.science/hal-04649909v1>

Submitted on 27 Nov 2024

HAL is a multi-disciplinary open access archive for the deposit and dissemination of scientific research documents, whether they are published or not. The documents may come from teaching and research institutions in France or abroad, or from public or private research centers.

L'archive ouverte pluridisciplinaire **HAL**, est destinée au dépôt et à la diffusion de documents scientifiques de niveau recherche, publiés ou non, émanant des établissements d'enseignement et de recherche français ou étrangers, des laboratoires publics ou privés.

A novel hydraulic bulge test in hot forming conditions

A. Boyer^{a,b}, N. Demazel^a, J. Coër^c, M. Carin^a, H. Laurent^{a,1,*}, M.C. Oliveira^b

^a*Univ. Bretagne Sud,*

UMR CNRS 6027, IRDL, F-56100 Lorient, France

^b*CEMMPRE, Department of Mechanical Engineering, University of Coimbra,
Polo II, Rua Luís Reis Santos, Pinhal de Marrocos, 3030-788 Coimbra, Portugal*

^c*NAVAL GROUP - Lorient*

Avenue de Choiseul, F-56311 Lorient, France

Abstract

A novel hydraulic bulge test device was developed to evaluate high temperature biaxial stress-strain curves of quenchable boron steel sheets. The work mainly focuses on the resistance heating designed to assure a homogeneous temperature field in the dome area of the circular blank where the hydraulic pressure will be applied. The practical hot stamping conditions, including the heating and cooling steps, were reproduced to perform hydraulic bulge tests on the Usibor[®]1500P steel for a temperature range between 700 to 900°C, after an austenization step at 900°C. Stress-strain curves were obtained from these expansion tests using the data extracted with a laser profilometer, due to the difficulties associated with the use of Digital Image Correlation at such high temperatures. Although the profilometer is a compromise solution, the comparisons between tensile and biaxial stress-strain results enable to verify the feasibility of the new device for the evaluation of the stress-strain curves at a high temperature in a biaxial state. The results point-out that, besides the difficulties with the acquisition of the strain fields and in the strain-rate control, there are also challenges in the interpretation of the metallurgical evolutions that can occur during the tests, which can affect the biaxial flow curves.

Keywords: Hydraulic bulge test, Hot stamping, Heat treatable steel, Formability test, High temperature

*Corresponding author

Email address: herve.laurent@univ-ubs.fr (H. Laurent)

¹Univ. Bretagne Sud,

UMR CNRS 6027, IRDL, F-56100 Lorient, France

Tel:(33) 2 97 87 58 11

1. Introduction

In order to provide flow stress curves and forming limits for hot steel metal forming simulations up to high strain levels, knowledge of the thermo-mechanical behaviour of the materials is of the up-most importance. The mechanical properties of boron alloy steels after forming at elevated temperatures were studied by many researchers. [Karbasiyan and Tekkaya \(2010\)](#) showed the potential of the hot stamping procedure by summarizing the thermal, mechanical and microstructural aspects of this material and gave the technological aspects of the procedure. [Merklein and Lechler \(2006\)](#) reported the flow stress of hot-stamped 22MnB5 steels and its dependency on temperature in uniaxial tensile conditions. [Li et al. \(2019\)](#) developed a procedure for the constitutive parameters identification for boron steels under hot conditions, based on Digital Image Correlation (DIC) assisted tensile tests. However, the information on properties obtained at elevated temperatures under biaxial stress state, using the hydraulic bulge test on this kind of materials is very limited.

As shown by [Lăzărescu et al. \(2011\)](#), the biaxial bulge test under hydraulic pressure, enables the determination of the flow stress curves of sheet metals up to high strain levels before the occurrence of necking and fracture. Therefore, as studied by [Bleck and Blumbach \(2005\)](#), it enables the definition of the hardening behaviour up to large plastic deformations, when compared with the ones attained in the uniaxial tensile test. [Koç et al. \(2011\)](#) showed also that the biaxial stress mode is also very interesting because it is the major deformation mode in many sheet forming processes. In this context, [Alharthi et al. \(2018\)](#) used the hydraulic bulge test to obtain the value of one of the key material parameters required to define most advanced yield functions, the biaxial yield stress. Finally, this test provides a way to obtain the expansion mode of the Forming Limit Diagram (FLD), as for example in the work of [Wu et al. \(2016\)](#).

In the hydraulic bulge test, the sheet (square or circular) is clamped between a circular die and a blank-holder, as shown in Figure 1. When a pressure p is applied to the fluid in the lower chamber, the sheet is bulged into the cavity of the die. [ISO16808 \(2014\)](#) standard recommends that the ratio between the sheet thickness, t , and the die diameter, D , to be equal to or lower than $1/33$. The clamping force between the die and the blank-holder has to be high enough to prevent the sliding of the sheet to the die cavity. Therefore, sometimes a drawbead is used to prevent the movement of the sheet in the clamped region, as shown by [Kaya et al. \(2008\)](#). The advantage

39 of this test when compared to the Nakazima or Marciniak tests is that the
 40 sheet is formed into a hemispherical geometry without using a punch. Thus,
 41 the deformation is not affected by friction. These tests are used to evaluate
 42 the materials formability while the bulge test enables also the evaluation of
 43 the stress-strain curves.

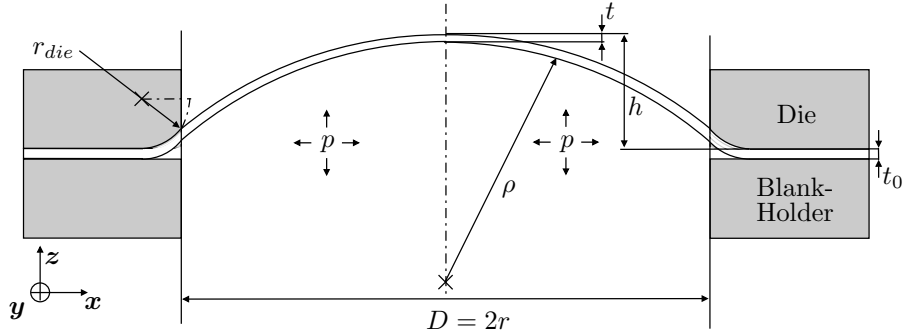


Figure 1: Principle of the biaxial bulge test (adapted from Lafilé et al. (2021)) and dimensional parameters used in this study (cross-sectional view).

44 Several hydraulic bulge tests devices have been developed during the last
 45 twenty years to perform the analysis in warm and hot conditions. Most of
 46 these devices were developed to test lightweight alloys, such as aluminium
 47 and magnesium alloys, in warm conditions. The heating technologies typi-
 48 cally used to reach temperatures inferior to 600°C are hot oil bath, cartridge
 49 heaters and furnaces. Lee et al. (2013) proposed a testing device for tem-
 50 peratures up to about 125°C where only the oil is heated. In Ayres and
 51 Wenner (1979), samples of AA5182-O aluminium alloy were tested while
 52 submerged in a hot circulating oil bath, whereas the tools were heated by
 53 cartridge heaters, up to a temperature of 200°C . In other studies, the die,
 54 blank-holder and blank were all submerged in a liquid, heated by cartridge
 55 heaters installed in various locations inside the tools. For example, Kaya
 56 et al. (2008) conducted tests on the AZ31-O magnesium alloy for tempera-
 57 ture up to 225°C . Groche et al. (2002) conducted tests on the EN AW-5083
 58 and EN AW-6016 alloys with temperatures up to 250°C and determined the
 59 biaxial flow stress curves for these materials. Using the same principle, other
 60 researchers explored the biaxial hydraulic bulge tests at warm temperatures.
 61 In Koç et al. (2011), the AA5754 aluminium alloy was studied, for a maxi-
 62 mum temperature of 260°C , while in Mahabunphachai and Koç (2010) two
 63 aluminium alloys: AA5052 and AA6061, were studied up to 300°C . Li and
 64 Ghosh (2004) studied the biaxial warm forming behaviour of three automo-
 65 tive aluminium sheet alloys for a temperature range between 200 and 350°C .

66 To obtain the FLD of these alloys, the tools were heated using embedded
67 heaters while the blank was heated by convection. Using the same principle,
68 the formability of the AA5083 alloy was tested at 550 °C by [Banabic et al.](#)
69 (2005), under a constant strain rate, by controlling the bulging gas pressure,
70 for circular and elliptical dies and by the cone-cup testing method.

71 [Abu-Farha and Hector \(2011\)](#) developed a pneumatic stretching test
72 where the forming die assembly is placed in a heating chamber. They ex-
73 plored sheet orientation effects on the hot formability limits of two lightweight
74 materials: the AA5083 aluminium and the AZ31B magnesium alloys, up to
75 450 °C. [Liu et al. \(2015\)](#) used a resistance furnace to heat the tools and sam-
76 ple to determine the hardening curves of an AA7075 sheet, for temperatures
77 lower than 280 °C. [Shao et al. \(2018\)](#) determined the FLDs for an AA5754
78 alloy at various temperatures (200 to 300 °C) and forming speeds (20 to 300
79 mm s⁻¹) by setting up the test tool in a hot furnace, to create an isothermal
80 environment.

81 Concerning temperatures higher than 600 °C, furnaces are still used but
82 induction and resistance heating methods are emerging. For example, [Bar-](#)
83 [iani et al. \(2008\)](#) presented a stretching-forming Nakazima test, for evaluating
84 the formability limits in the hot stamping of high strength steels, for tem-
85 peratures up to 700 °C. In this case, the metal blanks and the tools are
86 heated by induction. [Shao et al. \(2016\)](#) used a resistance heating method,
87 to develop a novel biaxial testing system in a Gleeble testing machine based
88 on a type of cruciform specimen to evaluate the forming limits under hot
89 stamping conditions for boron steel and AA6082 aluminium alloys. [Li et al.](#)
90 (2012) evaluated the effect of applying a pulse current to heat a rectangular
91 sheet by developing a free bulging test that was applied to AZ31 Mg alloy
92 at 400 °C. With the same heating method, [Wang et al. \(2018\)](#) studied the
93 superplastic gas bulging of Ti₂AlNb alloy at 980 °C. Finally, by using resis-
94 tance heating by Joule effect of a rectangular sheet, an hot-gas-bulge test was
95 designed by [Braun et al. \(2016\)](#) to characterize hot stamping steel 22MnB5,
96 at temperatures up to 900 °C and strain rates up to 0.5 s⁻¹.

97 This resistance heating technique (or conduction heating), as proposed by
98 [Mori et al. \(2017\)](#), is a very attractive method to heat a thin metallic sheet.
99 Resistance heating is a promising alternative to roller-hearth furnaces, which
100 are commonly used for hot stamping since it provides very high heating
101 rates, as shown by [Mori et al. \(2020\)](#). If the output of the power supply
102 is sufficient, [Maeno et al. \(2019\)](#) showed that it is a very attractive way
103 for heating sheets while avoiding metallurgical modifications (like oxidation
104 and decarburization) in the case of heat-treatable materials. Additionally,
105 resistance heating seems more suitable to use an optical measurement device,
106 than a furnace or an inductor. However, the temperature distribution in

107 the heated specimen is in general less homogeneous, when compared to a
108 specimen which is heated by a furnace, as was observed by [Braun et al.](#)
109 [\(2014b\)](#). Indeed, [Liang et al. \(2014\)](#) noticed that if the blank has a variable
110 current cross section, then the temperature field can be heterogeneous with
111 severe overheatings.

112 The Joule heating process is already used in industry, but often only
113 applied to blanks with long and narrow geometry, such as: rectangular blanks
114 studied by [Mori et al. \(2005\)](#) for ultra-high strength steels, and by [Maeno](#)
115 [et al. \(2018\)](#), for hot stamping steel; pipes, rods, wires by [Kolleck et al. \(2008\)](#);
116 and L-angle profiles by [Deng et al. \(2018\)](#). This technique was also used by
117 [Nakagawa et al. \(2020\)](#) for non-rectangular steel sheets by local preheating
118 and in the hot stamping of a front bumper by [Liang et al. \(2021\)](#). [Demazel](#)
119 [et al. \(2021\)](#) adapted this technology to any blank shape, as exemplified for a
120 windscreen upright blank, by splitting it into several rectangular strips heated
121 by five electrical generators. [Santos et al. \(2014\)](#) used also this method to
122 assist the friction stir welding.

123 During the bulge test, the temperature field in the blank should be as
124 uniform as possible, because the objective is to determine the stress-strain
125 relationship in biaxial state at high, constant, temperatures. In this case,
126 there are also challenges related with the measurement of the evolution of
127 the bulge radius and polar thickness of the specimen. Nowadays, the DIC
128 technique is classically adopted for strain measurement during bulge tests,
129 as mentioned by [Mulder et al. \(2015\)](#). DIC enables full-field strains to be
130 measured at different stages of forming by comparing the digital images of
131 a pattern sprayed or a grid etched on the specimen, even for temperatures
132 up to 500 °C as used by [Shao et al. \(2016\)](#) or for very thin sheets by [Sène](#)
133 [et al. \(2013\)](#). However, the use of high temperature conditions gives rise
134 to difficulties when using DIC systems. Indeed, the pattern required for
135 using this measurement method needs to withstand high temperature and
136 large stretching, without sliding or cracking. Thus, currently, the DIC at very
137 high temperature and under large deformation conditions remains difficult to
138 control, as mentioned in [Aksenov and Sorgente \(2020\)](#). Thus, an alternative
139 technique, using a laser profiler is tested in this work, as already done by our
140 team in [Boyer et al. \(2019\)](#), to obtain the stress-strain curve from a biaxial
141 test, for an AA6061-T6 aluminium alloy at 150 °C.

142 As other material characterisation experiments, the bulge test might also
143 be influenced by non-isothermal process conditions and deviations in the
144 testing strain rates. Indeed, in the majority of the hydraulic bulge methods
145 at high temperature presented before, direct measurements of the specimen
146 pole temperature revealed non-isothermal condition during bulging, as in
147 the work of [Wang et al. \(2010\)](#) and that it is difficult to maintain a constant

148 strain rate during the experiment, as mentioned in [Jocham et al. \(2017\)](#).
149 In fact, this difficulty is known since the early work of [Jovane \(1968\)](#) and
150 some approaches have been proposed. In this context, [Dutta and Mukherjee](#)
151 [\(1992\)](#) proposed an analytical equation to describe the evolution of pressure
152 with time for the bulge test. [Banabic et al. \(2005\)](#) used this equation to
153 describe the free bulging stage of the test performed with a conical die. In
154 this work, the authors also proposed analytical pressure-time evolutions for
155 bulging with circular and elliptic dies. More recently [Suttner and Merklein](#)
156 [\(2016\)](#) suggested using strain control with DIC system.

157 If the extent of these non-perfect process conditions is significant, [Braun](#)
158 [et al. \(2014a\)](#) proposed to determine the biaxial flow curve by inverse mod-
159 eling. [Aksenov and Sorgente \(2020\)](#) used in their work, a double-step nu-
160 merical procedure that allowed them to calculate the stress-strain curves for
161 constant strain rates, in the case of a superplastic Alnovi-U aluminium alloy
162 in conditions of biaxial tension at 500 °C.

163 In summary, there are three major challenges in the acquisition of the
164 biaxial stress-strain curves from hydraulic bulge tests, at high temperature:
165 (i) a heating method that assures a homogeneous temperature field in the
166 dome area; (ii) a procedure that enables the measurement of curvature and
167 thickness (or principle strains) evolutions at the pole; and (iii) a procedure
168 to assure a constant strain rate in the dome area during bulging. In this
169 work, an additional challenge is addressed: reproducing industrially relevant
170 hot forming conditions for the boron steel Usibor[®]1500P, which includes
171 heating at 900 °C to ensure a complete austenization, as highlighted in [Ven-](#)
172 [turato et al. \(2017\)](#). Therefore, it is mainly focused on the development of
173 a direct resistance heating technology, by Joule effect, applicable to circular
174 blanks. As previously mentioned, Joule effect heating is easily achievable
175 for a rectangular sheet, it is quite challenging to establish a method allow-
176 ing rapid and homogeneous heating of a circular blank. The isolated metal
177 tools required to clamp the blank lead also to thermal conduction, which
178 introduce a radial thermal gradient. Thus, the challenge of using Joule effect
179 heating is to obtain a uniform temperature field on the blank area where the
180 hydraulic pressure will be applied. This is particularly difficult when con-
181 sidering hot forming conditions such as those used for boron steels, due to
182 the high temperature required. Therefore, a numerical thermoelectric model
183 from COMSOL Multiphysics[®] was built to help establishing the conditions
184 for the heating procedure to be adopted. This model was also applied to
185 enable the control of the temperature throughout the duration of the test.
186 Thus, unlike other types of resistance heating systems in bulge apparatus
187 (*e.g.* [Braun et al. \(2016, 2014b\)](#)), it is possible to adjust and control the
188 temperature of the blank during the forming step. Moreover, it is possible to

189 reproduce hot stamping conditions by controlling the heating rate, soaking
190 time and pressure rate.

191 The remainder of the manuscript is organized as follows. Section 2
192 presents the chemical composition of the 22MnB5 alloy and the thermal
193 properties required for the development of the numerical resistance heating
194 model. In section 3, the COMSOL Multiphysics[®] thermoelectric model is
195 described and used to establish a configuration that enables heating of the
196 circular blank in the hydraulic bulge test. Then, the experimental set-up is
197 described. A comparison between experimental and numerical temperature
198 distributions during the heating phase is presented in order to validate the
199 heating solution proposed. In section 4, the methods used to extract the
200 stress-strain curves from expansion and uniaxial tensile tests are presented.
201 A subsection is devoted to the many difficulties encountered in applying DIC
202 techniques, which justify the adoption of a laser profilometer as a compromise
203 alternative. Note that, the comparison of results obtain with DIC and the
204 laser profilometer was previously reported by our team in [Boyer et al. \(2019\)](#) ,
205 for an AA6061-T6 aluminium alloy at 150 °C. The aim of this subsection is to
206 systematize the issues that need further improvements, in order to be able to
207 apply DIC techniques at high temperatures. The biaxial stress-strain curves
208 of the Usibor[®]1500P are compared with the ones obtained using tensile tests
209 on a Gleeble machine in section 5. This section includes some explanations
210 for the differences observed in the results obtained under tensile and biaxial
211 conditions. Finally, the main conclusions are summarized in section 6.

212 2. Material

213 The boron/manganese micro-alloyed steel used in this study is an
214 Usibor[®]1500P, produced by ArcelorMittal, with initial nominal thickness
215 values of $t_0=0.9$ mm and $t_0=1.0$ mm. The chemical composition of this steel
216 is given in Table 1.

| C | Mn | B | Si | P | Cu | Ni | Cr | Al | Ti | Mo |
|------|------|-------|------|-------|------|------|------|------|-------|--------|
| 0.22 | 1.23 | 0.004 | 0.25 | 0.008 | 0.03 | 0.02 | 0.20 | 0.03 | 0.037 | < 0.02 |

Table 1: Chemical composition (wt.%) of the Usibor[®]1500P steel.

217 The sheets of this quenchable steel are usually protected from oxidation
218 and decarburization with an Al-Si layer, basically composed of 90% alu-
219 minium and 10% silicon. In this study, the sheets are covered with 80 g m⁻²
220 of Al-Si coating, *i.e.* the thickness layer is between 23 and 32 μm as men-
221 tioned in [Demazel et al. \(2018\)](#).

222 The steel thermal properties were obtained from the ArcelorMittal
 223 database (for further details refer to Demazel (2018)). The evolutions in
 224 function of temperature of the density ρ , the thermal conductivity k , the
 225 specific heat C_p , the electrical conductivity σ_e and the emissivity ε are pre-
 226 sented in Figure 2.

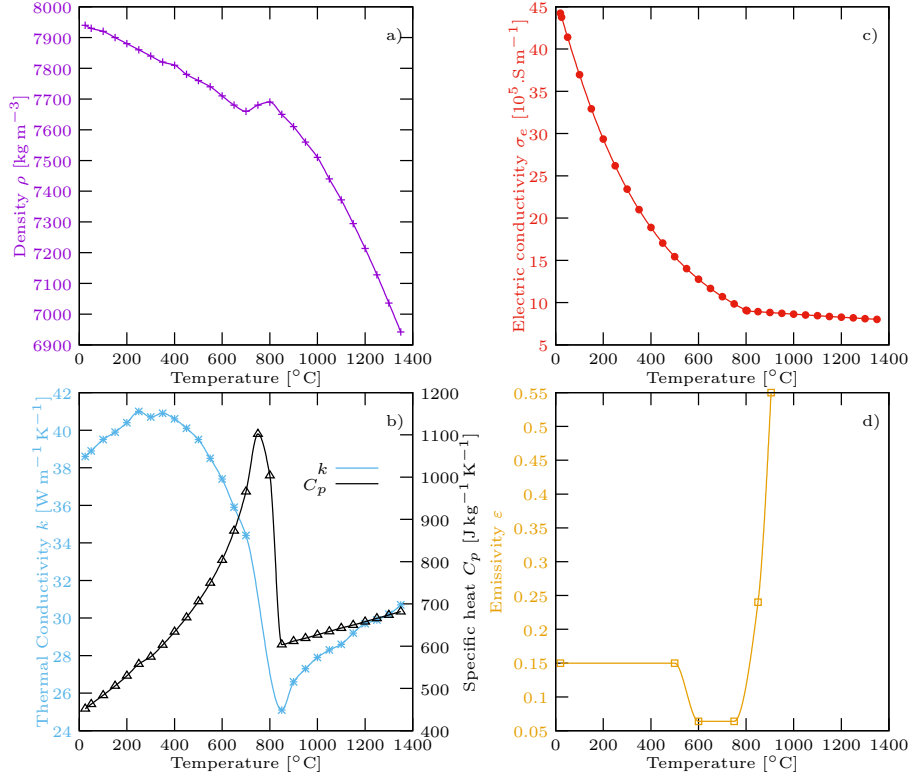


Figure 2: Thermal properties: a) Density ρ ; b) Thermal conductivity k and specific heat C_p ; c) Electrical conductivity σ_e and d) Emissivity ε .

227 The density decreases with the increase of temperature, except for the
 228 small increase that occurs at the transformation temperature into austenite
 229 ($\approx 730^\circ\text{C}$). The thermal conductivity presents a strong decrease during the
 230 austenitization stage, but afterwards shows an increasing trend. The spe-
 231 cific heat increases with temperature but suddenly, after the austenitization
 232 stage it decreases, due to the fact that this evolution takes into account the
 233 enthalpy of the phase transformation. As for many other metallic materials,
 234 the electrical conductivity decreases with the increase of temperature. The
 235 emissivity of the Usibor[®]1500P steel coated with the Al-Si layer depends on
 236 the alloying kinetic. It shows that the emissivity is low below 500°C , de-
 237 creases between 500 and 600°C , and then increases for temperatures higher

238 than 750 °C. For the electro-thermal model presented below, the emissivity
 239 is assumed as constant for temperatures higher than 900 °C. The decrease of
 240 the emissivity is due to the optical behaviour of the coating around 600 °C,
 241 since the blank surface appears as reflective as a mirror when the coating is
 242 melting. The increase after 750 °C is linked with the progress of the coating
 243 alloying to the steel surface, to form a protective layer against oxidation.

244 3. Design of the bulge test device

245 In order to have an uniform temperature field in the inner circular part
 246 of the blank, an electro-thermal coupled model, implemented in the finite
 247 element software COMSOL Multiphysics[®] was built to define the resistance
 248 heating system of the device. With this model, several parameters were tested
 249 and adjusted to attain a satisfactory configuration, such as the number, the
 250 shape, the position and the size of the electrodes, as well as the intensity
 251 and the time duration of the electrical current. The influence of the tools
 252 geometry on the cooling of the blank exterior perimeter and its effect on the
 253 temperature field in the central zone was also studied. The details about
 254 the numerical model are presented in this section. The integration of these
 255 numerical solutions in the new bulge test device is also described.

256 3.1. Resistance heating design

257 The principle of the hydraulic bulging setup used in this study is shown in
 258 Figure 3. This device is composed of a circular blank completely clamped on
 259 its perimeter between the die and the blank-holder. After the clamping, the
 260 blank is heated by Joule effect using electrodes and finally it is deformed by
 261 an inert pressured gas (argon). Both tools are supposed electrically isolated.
 262 The blank has an exterior diameter of 240 mm and the die diameter is $D =$
 263 $2r = 120$ mm.

264 The geometry of the 3D electro-thermal model is composed of the blank,
 265 the tools (die and blank-holder) and the electrodes. The temperature depen-
 266 dence of the thermal parameters of the blank follows the evolutions presented
 267 previously in Figure 2. The thermal problem is solved using the classical en-
 268 ergy conservation law:

$$\rho(T) C_p(T) \frac{\partial T}{\partial t} = \text{div}(\mathbf{k}(T) \cdot \text{grad}(T)) + Q_{Joule} \quad (1)$$

269 where \mathbf{k} is the thermal conductivity tensor (considered isotropic), T is the
 270 temperature of the blank surface and Q_{Joule} is the heat source induced by
 271 the Joule effect given by:

$$Q_{Joule} = \text{grad}^T(V) \cdot \boldsymbol{\sigma}_e(T) \cdot \text{grad}(V) \quad (2)$$

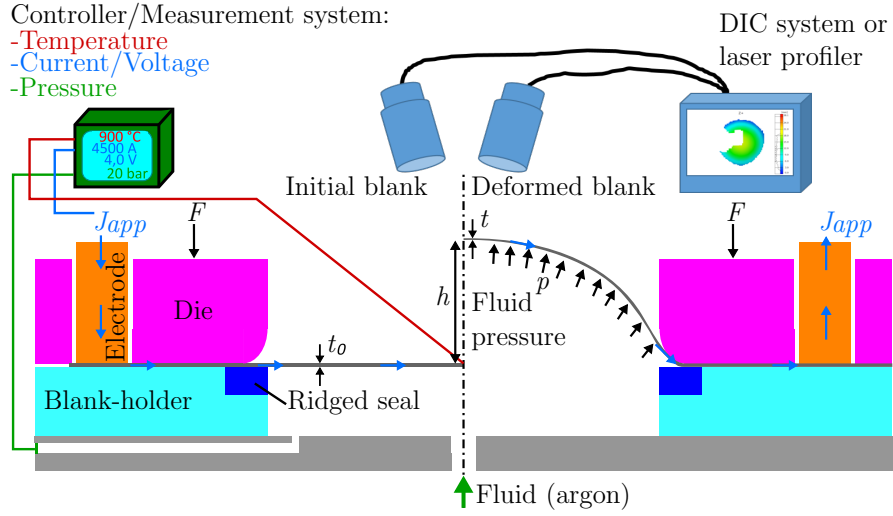


Figure 3: Principle of the hydraulic bulge test device with pressure/electrical/temperature controller and DIC optical measurement system or laser profilometer.

272 where σ_e is the electrical conductivity second order tensor (considered
 273 isotropic) and V is the electrical potential. The electrical problem is solved
 274 using the current continuity equation:

$$\text{div}(\mathbf{J}) = 0 \quad (3)$$

275 where \mathbf{J} represents the electrical current density vector, given by the local
 276 Ohm's law:

$$\mathbf{J} = \sigma_e(T) \cdot \text{grad}(V) \quad (4)$$

277 Convective losses are described by the Newton law:

$$-\mathbf{n} \cdot \boldsymbol{\varphi}_{conv} = h(T_{air} - T) \quad (5)$$

278 whereas radiative losses are described by the Stefan-Boltzmann law:

$$-\mathbf{n} \cdot \boldsymbol{\varphi}_{rad} = \varepsilon(T) \cdot \sigma_b (T_{ext}^4 - T^4) \quad (6)$$

279 where \mathbf{n} is the unit normal vector to the blank's surface, $\boldsymbol{\varphi}_{conv}$ and $\boldsymbol{\varphi}_{rad}$
 280 are the convective and radiative heat flux vectors, h is the heat transfer
 281 coefficient, σ_b is the Stefan-Boltzmann constant, $T_{air} = 20^\circ\text{C}$ is the air
 282 temperature and $T_{ext} = 20^\circ\text{C}$ is the temperature of the surrounding surface.
 283 These losses by radiation and convection are calculated assuming the blank
 284 as a grey body and constant convection heat transfer coefficients. The value
 285 used for h is assumed constant at $10 \text{ W m}^{-2} \text{ K}^{-1}$.

286 A condition of electrical insulation is used between the tools and the
 287 external surfaces of the blank, such as:

$$-\mathbf{n} \cdot \mathbf{J} = 0 \quad (7)$$

288 An input density current J_{app} is applied to the upper surfaces of the elec-
 289 trodes, as schematically illustrated in Figure 3, such as:

$$-\mathbf{n} \cdot \mathbf{J} = \pm J_{app} \quad (8)$$

290 The electrical current density between two surfaces in contact is evaluated
 291 by:

$$-\mathbf{n} \cdot \mathbf{J}_{cont} = \frac{(V_1 - V_2)}{ECR} \quad (9)$$

292 where \mathbf{J}_{cont} is the contact electrical density vector, ECR is the Electrical
 293 Contact Resistance coefficient and V_1 and V_2 are the electrical potentials of
 294 the two surfaces in contact.

295 The Joule effect due to the electrical contact resistance is taken into
 296 account with the following equations:

$$\begin{cases} -\mathbf{n} \cdot (\mathbf{k} \cdot \text{grad}(T_1)) = \frac{(T_2 - T_1)}{TCR} + (1 - \alpha) \frac{(V_1 - V_2)^2}{ECR} \\ -\mathbf{n} \cdot (\mathbf{k} \cdot \text{grad}(T_2)) = \frac{(T_1 - T_2)}{TCR} + \alpha \frac{(V_1 - V_2)^2}{ECR} \end{cases} \quad (10)$$

297 where TCR is the Thermal Contact Resistance coefficient, T_1 and T_2 are the
 298 temperatures of each surface in contact and α is the partition coefficient with
 299 a chosen value of 0.5 due to the metallic contact, as described in the work of
 300 [Rogeon et al. \(2008\)](#).

301 The choice of ECR and TCR values is a particularly delicate point, since
 302 they depend on the contact conditions, such as the imperfections of rough
 303 surfaces and the contact pressure between the two surfaces. In the work of
 304 [Blaise et al. \(2013\)](#), the TCR , the latent heat of the austenite to martensite
 305 transformation and the Koistinen-Marburger parameters are evaluated by an
 306 inverse method using results of a contact heating device in order to improve
 307 the accuracy of numerical simulations of the hot stamping process. [Pradille
 308 et al. \(2010\)](#) showed that the ECR decreases with the increase of temperature
 309 or pressure. [Terhorst et al. \(2016\)](#) studied lubricant and metallic contacts
 310 using experimental and numerical analysis. Their model used for TCR and
 311 ECR takes into account many dependencies such as the real contact surface
 312 area, the contact temperature and the contact pressure.

313 The contact resistance coefficients were estimated in this study using a
 314 device similar to the one presented in [Loulou et al. \(2006\)](#). As described

315 in Demazel (2018), a mean contact pressure between the electrodes and the
316 blank of 0.5 MPa was applied and the values of $ECR = 2.2 \times 10^{-7} \Omega \text{ m}^2$ and
317 $TCR = 6.5 \times 10^{-4} \text{ K m}^2 \text{ W}^{-1}$ were estimated. These values were validated by
318 comparing experimental with numerical results, when heating a rectangular
319 blank in Demazel et al. (2021).

320 Concerning the type of finite elements, after a numerical convergence
321 study, 3D tetrahedral elements with quadratic interpolation and average sizes
322 of $7.4 \times 10^{-5} \text{ m}$ for the blank, and $3.3 \times 10^{-2} \text{ m}$ for the tools, lead to the best
323 solutions. The maximum step time was set to 0.05 s.

324 In a preliminary study of Demazel et al. (2016), this electro-thermal model
325 showed that the use of one pair of electrodes to heat a circular blank results
326 in a heterogeneous distribution of the current flow, leading to an heteroge-
327 neous temperature field. According to the studies carried out at the Leibniz
328 University, by Behrens et al. (2015), one of the solutions to heat uniformly
329 a blank with a variable electrical current cross section is to use several pairs
330 of electrodes. Therefore, several combinations were numerically tested using
331 multi-electrodes combinations.

332 The solution that lead to an homogeneous temperature field in the centre
333 of the blank was obtained by using three pairs of electrodes, oriented at 60°
334 from each other, as shown in Figure 4 (see also Demazel (2018)). In this case,
335 each pair of electrodes, as described in Figure 5-a, is activated alternately,
336 by switching the pairs of electrodes in contact with the blank. After a pair
337 of electrodes has been active for a defined period t_{app} , it is inactivated, while
338 another pair supplies the power. This type of scheme for the electrical current
339 application aims to uniformly heat the central area of the blank and reduce
340 hot spots near the electrodes.

341 The influence of the electrodes geometry and their position in relation
342 to the tools was also studied with the numerical model. These parameters
343 mainly affect the hot spots in the areas of the blank around the electrodes.
344 The temperature may become higher than 600°C , which leads to the melting
345 of the Al-Si coating and a consequent degradation of the electrodes. To avoid
346 these hot spots, the electrodes must be located through the die to cool down
347 the blank zones around the electrodes. After several numerical trials, a good
348 solution was obtained with the geometry and the positions for the electrodes
349 inside the tools, as shown in Figure 4 (see Demazel (2018) for further details).

350 This configuration was used to study the influence of the electrical cycle
351 on the heating time and the temperature field in the central area of the
352 blank. As expected, the longer is the application time t_{app} and the higher
353 is the electrical current intensity, the faster is the heating. However, despite
354 the electrode position inside the tools, the electrical cycle has a considerable
355 influence on the maximum temperature attained in the blank areas located

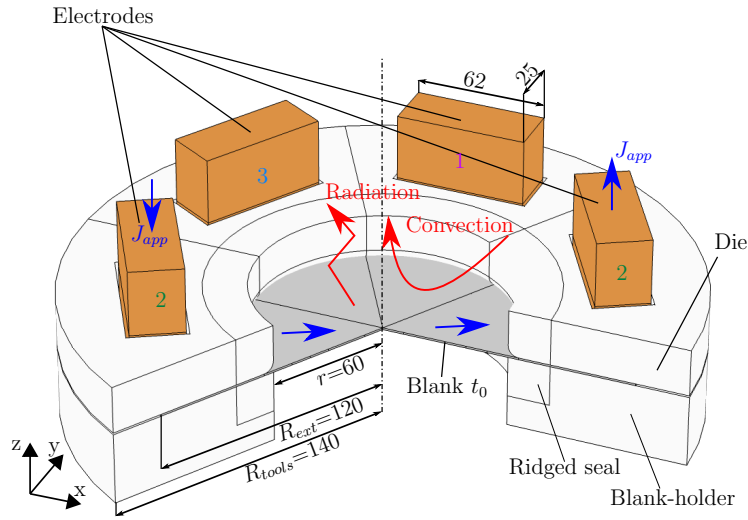


Figure 4: Final geometry of the device defined using the 3D COMSOL Multiphysics[®] model with electro-thermal coupling (dimensions in mm).

356 around the electrodes. Moreover, to obtain a uniform temperature field in
 357 the centre of the blank, the application time t_{app} must be short, to have a
 358 rapid rotation of the electrical current, associated with the switching of the
 359 electrodes. Thus, to avoid hot spots and to assure temperature uniformity, it
 360 is necessary to find a compromise between the application time and the total
 361 heating time. This needs also to take into account the final temperature,
 362 which in case of boron steel is 900 °C.

363 Figure 5-b presents an example of the electrical current application pro-
 364 posed for a total heating time of 50 s. This heating cycle is composed of two
 365 phases: heating and holding. During the heating phase of 34 s the applica-
 366 tion time t_{app} is 1.4 s with a current intensity that starts at about 4800 A and
 367 decreases to 4000 A, which then remains constant 20 s. During the tempera-
 368 ture holding phase, the current is maintained constant at about 4400 A and
 369 the application time t_{app} is reduced to 0.7 s in order to achieve a constant
 370 uniform temperature in the centre of the blank.

371 Figure 5-c shows the temperature field at the end of the heating cycle,
 372 showing that hot spots are avoided while a temperature of 900 °C is attained
 373 at the centre of the blank. A drop of 35 °C between the centre of the blank and
 374 the radius of 40 mm is observed therefore, it can be considered homogeneous
 375 in the central area, where the gas pressure will be applied. Circular isotherms
 376 are present due to the conduction cooling induced by the contact with the
 377 die and the blank-holder. Figure 5-d shows the evolution of the temperature
 378 at the centre of the blank as well as the maximum temperature near the

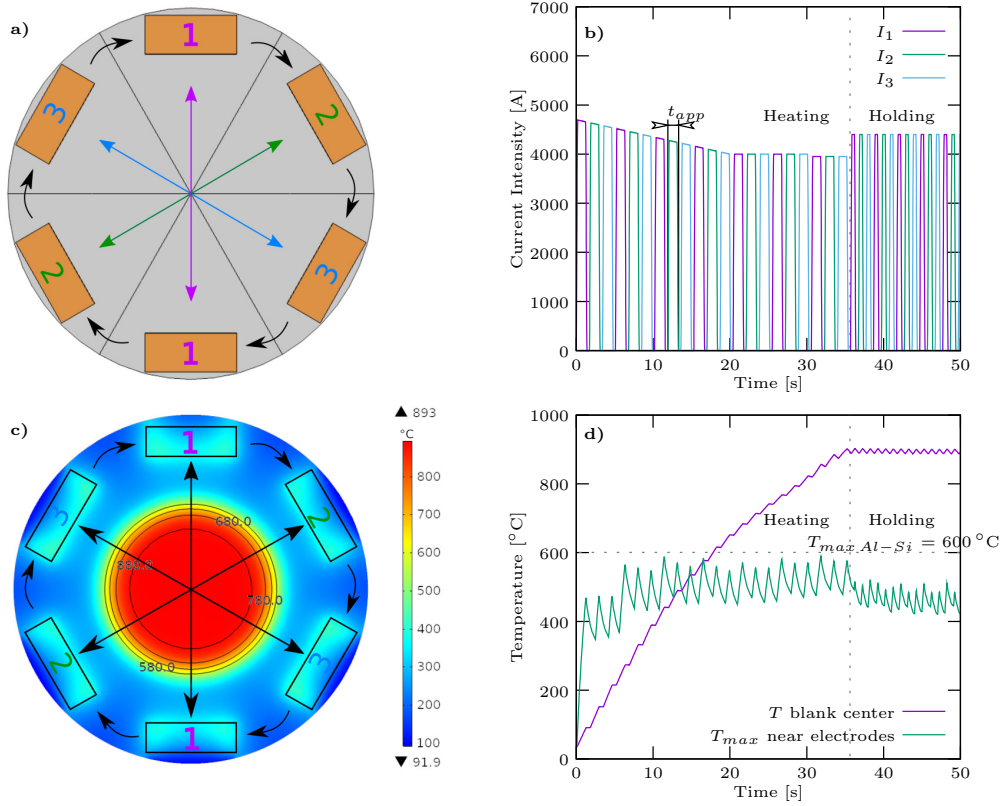


Figure 5: a) Schematic representation of the rotation of the electrical current in the three pairs of electrodes; b) Example of an evolution of the electrical current intensity I , applied in each pair of electrodes, during a heating cycle of 50s; c) Temperature field resulting from the electrical cycle shown in b) indicating the rotation motion of the electrodes; d) Temporal evolution of the temperature at the centre of the blank and of the maximum temperature of the blank near the electrodes.

379 electrodes resulting from the electrical cycle presented in Figure 5-b. The
 380 heating time to reached 900 °C is 35s and the temperature of the hot spots
 381 of the blank around the electrodes is maintained under 600 °C .

382 In summary, the feasibility of resistance heating to attain a high tem-
 383 perature, constant in a bulge test device has been demonstrated using this
 384 numerical model. The temperature in the centre area of the blank proves to
 385 be fairly homogeneous, allowing to perform the expansion operation with a
 386 constant temperature in this area. In the following section, the expansion
 387 device developed taking into account these results will be presented in detail.

388 *3.2. Experimental setup*

389 Based on the numerical study previously presented, a bulge test device
 390 was designed and constructed. The different components of this device are
 391 presented in Figure 6.

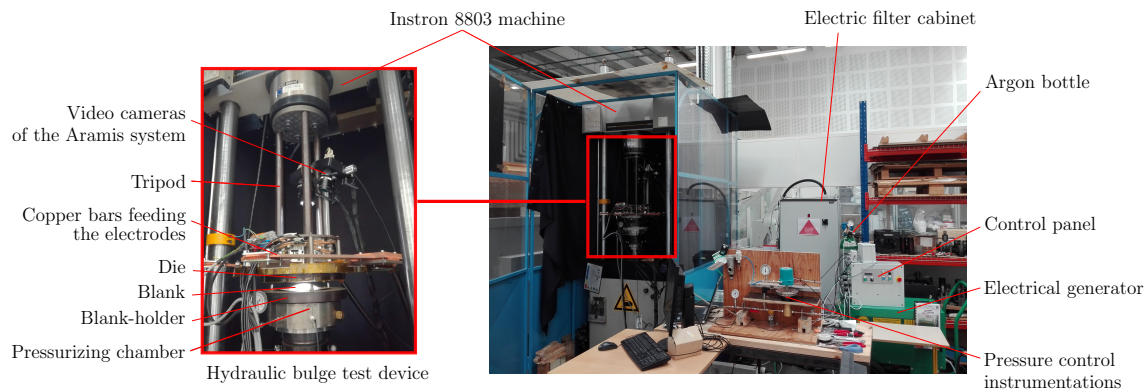


Figure 6: Details of the hydraulic bulge test setup with the different components of the device.

392 The device is composed of an electrical generator, which is supplied by two
 393 steps of the three-step network, in 400 V and 200 A, *i.e.* 80 kV A. The elec-
 394 trical generator can provide an alternative current with Root Mean Square
 395 (RMS) current up to 6000 A and a measured maximum power at the elec-
 396 trodes lower than 22 kW. It is associated with an harmonic filter cabinet,
 397 to reduce step imbalances resulting from the fact that the generator is sup-
 398 plied with two steps of the three-step network. The electrical current flow
 399 to the electrodes is ensured by a set of cables, blocks and braids in copper.
 400 A control panel commands the electrical current via a temperature control
 401 loop.

402 The test bench of the bulge-test, shown in the zoom of Figure 6, is placed
 403 in an Instron 8803 tensile test machine, equipped with a load cell capacity
 404 of 500 kN. The tools are split into an upper (die) and a lower part (blank-
 405 holder), linked to the tensile machine with the help of a tripod. Both the die
 406 and the blank-holder are made of steel, coated with a non conductive film
 407 to electrically insulate them. An additional layer of Miglasil[®], which is an
 408 electrical and thermal insulator, is added to improve the tools insulation.

409 At the beginning of the test, a compressive clamping force of 300 kN
 410 is applied to the sheet by the tensile machine. A steel ridged seal with a
 411 Klinger[®] flexible gasket assures the sealing of the pressure cavity (see Fig-
 412 ure 3). Double-acting pneumatic cylinders control each pair of electrodes,

413 enabling the rotational permutation of the electrical field. A contact pres-
 414 sure of 0.5 MPa is applied successively between each electrode and the blank.
 415 A type K thermocouple with a diameter of 250 μm is welded at 10 mm from
 416 the centre of the blank by capacitive discharge, allowing the monitoring of
 417 the blank's temperature. For that purpose, the intensity of the applied cur-
 418 rent is controlled by a double current intensity/temperature regulation loop,
 419 allowing to follow the temperature set-point associated with the temperature
 420 measurement obtained from the thermocouple.

421 Due to the high temperatures aimed in the tests, the blank is formed
 422 by pressurized argon gas. The pressure is applied via a TESCOM ER5000
 423 pressure controller. A pressure sensor (0 to 70 bar) located inside the cavity
 424 monitors the pressure. During the test, the deformation of the blank can
 425 be recorded by one of two kinds of non-contact measurement systems (see
 426 Figure 3). The first one is a stereoscopic system (two CCD cameras, with
 427 GOM ARAMIS DIC system) to measure the surface of the dome apex (see
 428 Figure 6). The second one is a laser profilometer (Keyence LJ-V7200). In
 429 this case, only a section passing through the centre of the top of the dome is
 430 measured. More details about this bulge-test device and its design can also
 431 be found in Demazel (2018).

432 3.3. Preliminary test analysis

433 In this section, the detailed analysis of a preliminary test of heating and
 434 bulging a boron blank, with the expansion device at 700 $^{\circ}\text{C}$, is performed.
 435 The comparison between the experimental and numerical results of tempera-
 436 ture evolution is also presented, in order to highlight the control parameters
 437 involved in the experimental setup. Figure 7 shows the blank obtained at
 438 the end of the test.

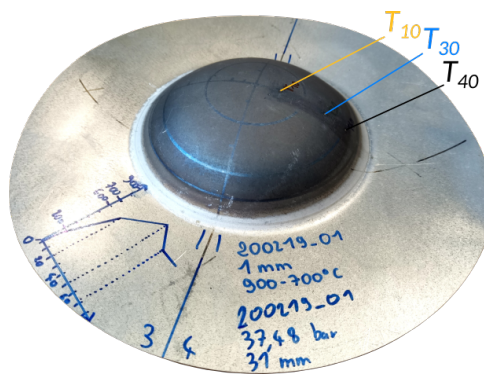


Figure 7: Blank after preliminary test at 700 $^{\circ}\text{C}$ with indication of the position of the three thermocouples T_{10} , T_{30} and T_{40} .

439 To analyse the distribution and evolution of the temperature during the
 440 heating and expansion steps, three type *K* thermocouples were placed at 10,
 441 30 and 40 mm from the centre, as shown in Figure 7, and labelled T_{10} , T_{30}
 442 and T_{40} . The heat treatment imposed during this test, described by the T_{set}
 443 temperature, is composed of a heating step up to 900 °C in 50 s, a soaking
 444 during 10 s and a cooling to 700 °C, as presented in Figure 8. The expansion
 445 step begins at 74 s.

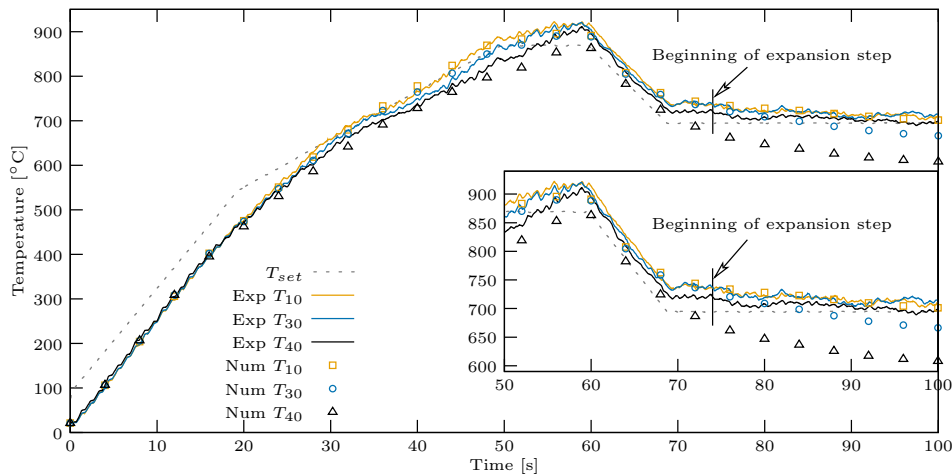


Figure 8: Comparison between experimental and numerical results of temperature evolution for the three thermocouples during the heating, holding and expansion steps for the bulge test at 700 °C.

446 Note that a study performed by ArcelorMittal (Demazel (2018) page 34)
 447 has shown that a heating time between 2 and 10 s, and a soaking time of
 448 at least 7 s lead to the target mechanical properties after quenching, which
 449 means that the austenitization is completed and that the full martensitic struc-
 450 ture is achieved after quenching. Maeno et al. (2020) shown also that, in
 451 case of hot bending of a 22MnB5 specimen heated by resistance heating, the
 452 microstructure is entirely martensitic after quenching for a soaking time be-
 453 tween 5 and 10 s. Kolleck et al. (2009) shown that similar properties can be
 454 reached with induction heating in comparison to convective heating, for an
 455 uncoated 22MnB5 steel, with a much shorter heating time. In their case, due
 456 to the configuration of the induction-heating device, the shortest heating time
 457 guaranteeing austenitization was 35 s. Löbbe et al. (2016) also considered an
 458 uncoated 22MnB5 steel and an induction heating device to analyze the in-
 459 fluence of the austenitization temperature (between 950 °C and 1100 °C) and
 460 dwell times (3 and 10 s) on the mechanical properties. The results show that
 461 a fully martensitic microstructure always develops. Moreover, it is consensual

462 that the austenitization and homogenization process is strongly dependent
 463 on the microstructure constitution. In this context, Hou et al. (2021) ana-
 464 lyzed the effect of rapid heating on the microstructure and tensile properties
 465 of a novel uncoated, oxidation-resistant, press-hardening steel, comparing its
 466 properties to the ones obtained with a conventional coated 22MnB5 steel.
 467 The results show that a minimum soaking time of 120 s is required to achieve
 468 complete austenitization of the novel steel. Nevertheless, the steel under anal-
 469 ysis presents no boron, which is the element that influences the hardenability
 470 the most, since it slows down the conversion into softer microstructures (Kar-
 471 basian and Tekkaya (2010)).

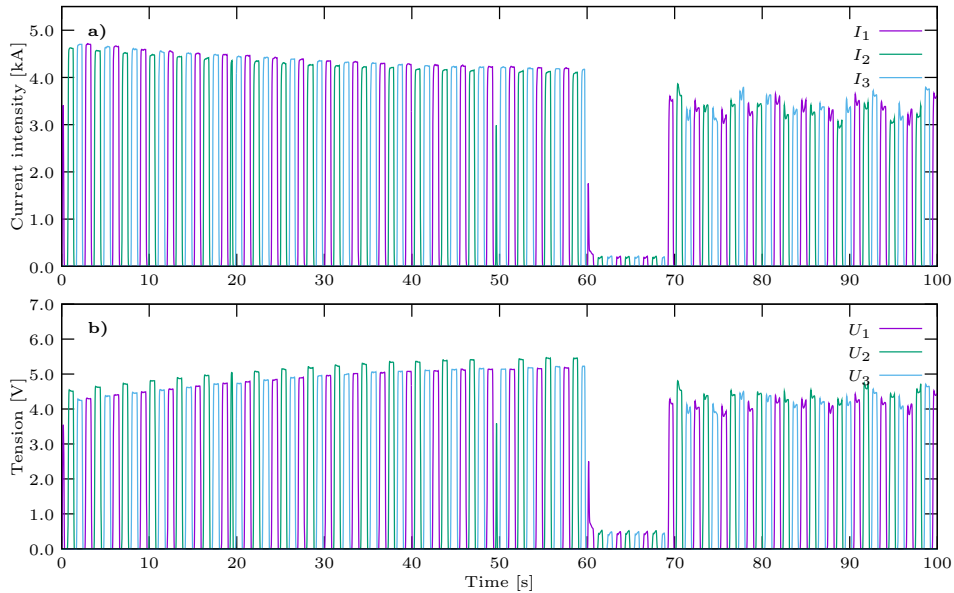


Figure 9: Temporal evolution during the preliminary test of: a) the experimental current in the three pairs of electrodes and imposed in the numerical simulation and b) the voltages measured in the three pairs of electrodes.

472 During the test, the alternative current delivered by the electrical genera-
 473 tor was managed by the PID controller to match the T_{set} temperature and the
 474 RMS current was recorded. The current profile delivered by the three pairs
 475 of electrodes is shown in Figure 9-a, while Figure 9-b presents the voltages
 476 measured under the pairs of electrodes. This allowed the comparison of the
 477 experimental temperature with the numerical results. For that, the current
 478 profile shown in Figure 9-a, was imposed in the numerical model. A constant
 479 application time, t_{app} of 0.7 s is used during this test. This means that the
 480 application time t_{app} had to be reduced when compared to the heating step

481 of the numerical study presented in section 3.3, in order to improve the tem-
482 perature homogeneity and especially to avoid hot spots near the electrodes.

483 The heating step presents two different slopes in the temperature control
484 loop, due to the constraints of the electrical generator used and the high
485 influence of the integral term of the PID controller (see Figure 8). The
486 second slope is less steep than the first because the power of the generator
487 is not sufficient to heat up as quickly, due to the endothermic reaction of
488 the austenitization and the increase of thermal losses at high temperature.
489 Therefore, the lower slope helps avoiding an increase of the integral term
490 that leads to an overheating of the central area of the blank.

491 Figure 7 shows that the blank presents a gradual change of color from the
492 centre to the outer edge. This evolution gives information on the thermal
493 history of different positions of the blank and is indicative of an homogeneous
494 temperature in its centre. Beyond the thermocouple T_{40} location, the color
495 of the blank changes, which corresponds to a high thermal gradient due to
496 the cooling by the contact with the tools (see also Figure 8).

497 Figure 8 presents the comparison between the numerical and experimen-
498 tal temperature evolutions for the three thermocouples. The results show
499 a good correlation during the heating step, with a maximum deviation of
500 30°C at 60 s, for thermocouple T_{40} . After the cooling step, the gap between
501 the measured and calculated temperatures for T_{40} gradually increase. This
502 can be related with the fact that the simulation does not take into account
503 the bulging deformation of the blank and, accordingly, the evolution of the
504 geometry (especially the thickness decrease and the increase of the distance
505 between electrodes passing through the blank centre, during the expansion
506 step). However, the correlation between measured and calculated tempera-
507 tures at the centre of the blank remains good.

508 This comparison shows that the numerical model results are consistent
509 with the experimental ones. In essence, the model allowed the definition of
510 the geometrical characteristics of the device, including size and position of the
511 pairs of electrodes, as well as the global electrical parameters necessary for
512 heating the sheet. It turns out to be particularly predictive: the parameters
513 selected for the electrical and thermal contact resistances make it possible
514 to obtain numerical results in agreement with the experimental ones. The
515 advantage of the resistance heating method is also demonstrated, because
516 the results show that this method allows to control the temperature of the
517 blank also during the expansion step. Therefore, it is possible to reproduce
518 almost all the steps of the hot stamping conditions: the heating and soaking
519 times and the temperature during the expansion. The cooling rate to attain
520 the temperature of the expansion step is not currently controlled. In the
521 future, cooling devices could also be envisaged.

522 4. Experimental methods

523 In this section, the methods used to extract the stress-strain curves from
524 the expansion tests, performed between 700 and 900 °C are presented. The
525 experimental conditions used to perform tensile test on the Usibor[®]1500P
526 steel, for the same range of temperature, in a Gleeble machine are also de-
527 scribed.

528 4.1. Expansion tests

529 The stress-strain curve is evaluated applying the membrane theory that
530 relates the stresses at the pole with the pressure, the radius of curvature
531 and the sheet thickness. There are mainly two possibilities as described, for
532 example, in Boudeau et al. (2018). One follows a more simple experimental
533 route, but requires the use of analytical models, which relate the evolution
534 of the radius of curvature and the sheet thickness with the only variable
535 measured: the pole height, h (see Figure 3). The other one requires the
536 acquisition of the geometry and strain distributions on the sheet surface
537 during the bulge test, *i.e.* can only be applied using a DIC system. At high
538 temperatures, DIC technique requires more experimental precautions, due
539 to the difficulties associated with the calibration of the video system, taking
540 into account the changes undergone by the surface of the blank with the
541 increase of temperature and the large deformations (see Figure 7).

542 In the following section, the main assumptions used to obtain the stress-
543 strain curves from the bulge-test results are recalled. Then, the difficulties
544 encountered when using a non-contact measurement system by DIC are de-
545 scribed. Thus, an alternative is proposed, based on using a laser profilometer
546 to measure the section of the dome during the expansion step. This requires
547 the application of analytical methods to extract the stress-strain curve, which
548 are also briefly recalled.

549 4.1.1. Evaluating the stress-strain curve using a DIC system

550 As the ratio between the initial thickness of the blank, which is either
551 $t_0 = 0.9$ mm or $t_0 = 1$ mm, and the die diameter $D = 120$ mm is lower than
552 $1/33$, as recommended by the ISO16808 (2014) standard (see Figure 4), the
553 bending stress occurring during the bulge test can be neglected. Thus, the
554 stress state at the centre of the sheet, assuming that the stress component
555 normal to the sheet surface, σ_3 , is equal to zero, can be obtained with the
556 aid of the membrane theory:

$$\frac{\sigma_1}{\rho_1} + \frac{\sigma_2}{\rho_2} = \frac{p}{t} \quad (11)$$

557 where σ_1 and σ_2 are the principal stresses in the sheet surface, which are
 558 assumed to be coincident with the rolling and the transverse direction. ρ_1
 559 and ρ_2 are the radii of curvature, at half thickness, in the same principal
 560 directions.

561 As mentioned in [Chen et al. \(2016\)](#), the stress state in the hydraulic
 562 bulge test can be considered in a first approximation as equibiaxial at the
 563 apex during deformation. For instance, the ISO 16808:2014 standard adopts
 564 the assumption that $\sigma_1 = \sigma_2 = \sigma_b$, where σ_b is the biaxial stress. This
 565 assumption, as explained by [Reis et al. \(2016\)](#), is valid for isotropic materials
 566 or orthotropic ones with similar properties for the rolling and transverse
 567 directions. In those cases, the radii of curvature also follow the assumption,
 568 such as $\rho_1 = \rho_2 = \rho$, which allow to simplify equation (11), such as:

$$\sigma_b = \frac{p\rho}{2t} \quad (12)$$

569 Although there is not a lot of information regarding the in-plane evolution
 570 of the Lankford coefficients of boron steels at high temperature, [Merklein
 571 et al. \(2007\)](#) showed that the austenitization reduces the grain orientation
 572 induced by the rolling process, leading to a planar anisotropy coefficient
 573 close to zero. Moreover, the flow stresses obtained from uniaxial tension
 574 tests performed at different orientations to the rolling direction present an
 575 fairly isotropic behaviour, as shown by [Merklein and Lechler \(2006\)](#). This
 576 allows adopting equation (12) to extract the stress-strain curves. The local
 577 thickness t of the blank's apex can be determined from the principal strains
 578 in the sheet plane, ε_1 and ε_2 , at the same location, using the condition of
 579 volume consistency during plastic deformation:

$$\varepsilon_t = -(\varepsilon_1 + \varepsilon_2) \quad (13)$$

580 Knowing the thickness strain ε_t and the initial thickness of the blank, t_0 , the
 581 thickness at the blank's apex can be estimated as follows:

$$t = t_0 \exp(-\varepsilon_t) \quad (14)$$

582 Note that the thermal expansion of the sheet in the bulge device causes
 583 the blank to expand, typically moving upwards, which maybe connected
 584 with the increase of the temperature of the air inside the cavity, causing
 585 its expansion. As the tests are performed under isothermal conditions, the
 586 thermal expansion can be assumed constant during the tests. Thus, the
 587 thermal expansion strain is calculated with the thickness strain at the instant
 588 the pressure start, $t_{i=P_{start}}$:

$$\varepsilon_{thermal} = \ln \left(\frac{t_{i=P_{start}}}{t_0} \right) \quad (15)$$

589 The current bulge strain ε_b is deducted from the total thickness strain as
590 follows:

$$\varepsilon_b = -\ln\left(\frac{t}{t_0}\right) + \varepsilon_{thermal} \quad (16)$$

591 This correction can overestimate the thermal strain since it also integrates
592 some elastic component. Nevertheless, the correction of the elastic strain
593 poses additional difficulties related with the knowledge of the evolution of the
594 material elastic properties with the temperature. Therefore, it was decided
595 to make no additional correction of the elastic component.

596 4.1.2. Difficulties of high temperature DIC

597 Outer surface 3D-DIC measurements are now classically used to monitor
598 the surface geometry of the bulge dome during the expansion test, as used
599 for example by Machado et al. (2012) for silicone elastomer and Lafilé et al.
600 (2021) for small size bulge tests. The use of two CCD cameras enables
601 the 3D-DIC system to capture the three-dimensional surface geometry and
602 displacements of the visible surface of the blank, allowing the acquisition of
603 the strain distributions on the sheet surface during the test. In this case, the
604 3D-DIC system is able to extract the major and minor strains, ε_1 and ε_2 , as
605 well as the radius of curvature ρ , *i.e.* the stress-strain curve can be directly
606 evaluated. However, in high-temperature conditions, 3D-DIC systems can
607 present some technical constrains, as explained by Aksenov and Sorgente
608 (2020).

609 DIC systems require a calibration, partly dependent on the image lu-
610 minosity and the reflective properties of the surface of the specimen. If an
611 evolution of the surface properties of the specimen occurs during the test, the
612 system can drift outside of its calibration window, leading to a monitoring
613 failure during the test. The basic principle behind DIC methods is the ap-
614 plication of a stochastic pattern or markings on the surface of the specimen
615 which will be tracked. This pattern needs to withstand high temperature
616 and large stretching without sliding off the blank's surface nor cracking.

617 Figure 10 illustrates the surface evolution of a blank during the heating
618 step of a high temperature bulge test, as seen by one of the cameras of
619 the DIC setup, equipped with a blue filter. The DIC system used is a GOM
620 ARAMIS 4M. The camera with a resolution of approximately 30 pixels mm^{-2}
621 recorded the motion of the specimen surface at the maximum frequency of
622 60 Hz. As explained in section 2, the blank surface is coated with the Al-Si
623 film, designed to alloy itself to the steel surface. The blank surface is clear
624 and reflective in its as received state (Figure 10-a). The thermal expansion
625 causes the blank to rise, this movement is observable by tracking the bright
626 spot on the surface of the blank in Figure 10-b. However, as previously

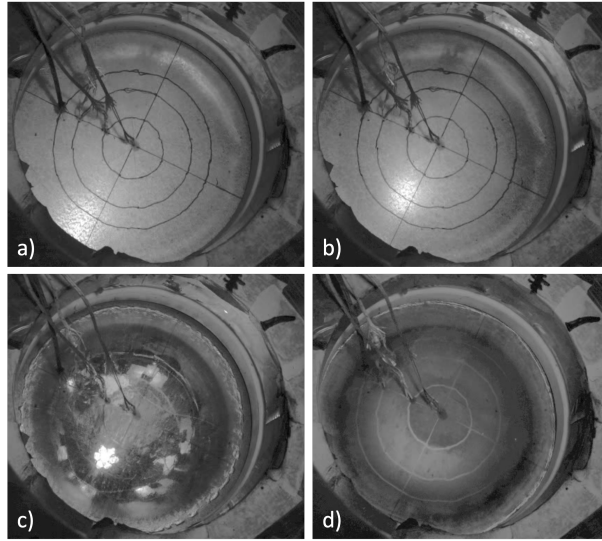


Figure 10: Evolution of the Usibor[®]1500P blank with Al-Si coating during the heating step of a bulge test: a) Initial conditions; b) 400 °C; c) 750 °C; d) 900 °C.

627 mentioned, during the melting of the coating, the blank surface appears as
 628 reflective as a mirror, as shown in Figure 10-c. In fact, the individual LEDs
 629 of the light used to illuminate the blank can be clearly distinguished for a
 630 brief moment once the blank reach 750 °C, as shown in Figure 10-c. After
 631 reaching the reflectiveness peak, the surface of the blank transitions to a dark
 632 and mat surface during the alloying of the coating to the steel. Figure 10-d
 633 shows this surface after the complete alloying of the Al-Si coating.

634 The colour transition observed is drastic enough to disturb any attempts
 635 to produce a conclusive and reliable DIC pattern for this high temperature
 636 range. In this context, Figure 11 shows the colour transition observed in a
 637 blank with an etched grid by electrolysis, which was also tested ineffectively.

638 Unfortunately, all the tests performed with various high temperature
 639 paints were also unsuccessful. The severity of the colour evolution of the
 640 blank is such that the thickness of paint required to mask it is detrimental
 641 to the integrity of the paint. In fact, a too large thickness for the paint
 642 weakens its overall elasticity, producing cracks in the paint during the bulge
 643 expansion. These cracks are reduced or do not appear during tensile tests
 644 using the same paint. Moreover, the Al-Si coating layer deposited on the
 645 Usibor[®]1500P, shows some movement during the expansion test, due to the
 646 electrical current imposed during the heating (visible in Figure 7). This can
 647 induce also movements of the paint pattern on the surface.

648 The nature of the bulge test setup forces the cameras to be on top of a

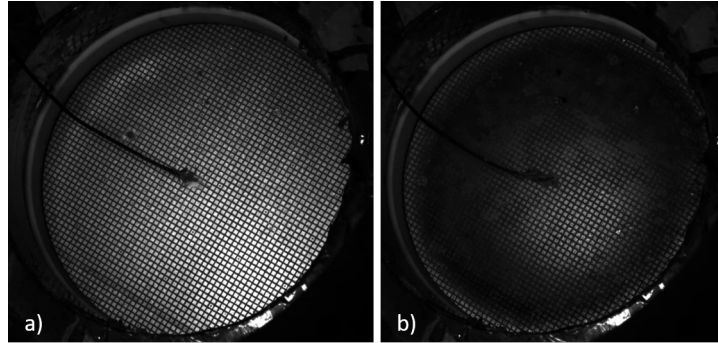


Figure 11: Colour transition during a bulge test on a grided blank by electrolysis, as seen by the 3D-DIC camera system: a) initial state; b) state at 900 °C.

649 cylindrical well (named tripod in Figure 6) which constrains the position of
 650 the light source between the cameras of the DIC system. Due to the distance
 651 between the light source and the blank, it is difficult to focus the light only
 652 on the sample. Reflections from the walls of the cylindrical well towards the
 653 blank can lead to bright spots, as shown in Figure 11-a) in the top left region.
 654 The nature of the dome also promotes the creations of shadows, as the pole
 655 height increases with pressure. Moreover, the evolution of the contrast of the
 656 blank affects the capability of the cameras: the optimal exposure parameters
 657 for the beginning of the test are incompatible with the parameters required
 658 for the conditions at the end of the test. Ultimately, the light exposure of
 659 the blank and the relative limited dynamic range of the cameras, makes it
 660 difficult to optimise the lighting for the complete duration of the test. An
 661 alternative approach could be to perform the calibration at high temperature
 662 during the homogenization step, which in that case needs to be long enough
 663 in time.

664 4.1.3. *Evaluating the stress-strain curve using a laser profilometer*

665 To avoid all the technical challenges associated with DIC, a laser pro-
 666 filometer was selected as an alternative. Nevertheless, the profilometer can
 667 only monitor a line passing through the centre of the blank. Correspondingly,
 668 when using this type of device, it is necessary to use analytical formulas to
 669 estimate the evolution of the thickness and the radius of curvature, during
 670 the test (see equation 12).

671 Several analytical models for the calculation of these variables have been
 672 proposed and tested for different experimental conditions and materials.
 673 Lăzărescu et al. (2011) highlighted the very good agreement between the re-
 674 sults obtained using DIC with the ones provided by analytical formula, for a

675 DC04 steel. On the other hand, [Boudeau et al. \(2018\)](#) work emphasizes that,
 676 for anisotropic materials, DIC is required for post-processing experimental
 677 results of the bulge test. The radius of curvature ρ can be determined as-
 678 suming that the blank as a spherical shape, dictated by the height of the
 679 pole's apex h and the die cavity radius r (see [Figure 1](#)). In these conditions,
 680 as suggested in [Hill \(1950\)](#), the radius of curvature can be determined as:

$$\rho_{Hill} = \frac{r^2 + h^2}{2h} \quad (17)$$

681 However, [Koç et al. \(2011\)](#) demonstrated that the radius of curvature was
 682 consistently underestimated by equation (17) on bulge tests performed on
 683 AA5754 and AISI 201 materials, either at room temperature and at 150 °C.
 684 [Panknin \(1959\)](#) assumed that the blank's dome is also part of a sphere, but
 685 considered the influence of the fillet radius r_{die} of the die's cavity (see [Figure](#)
 686 [1](#)), defining the radius of curvature as:

$$\rho_{Panknin} = \frac{(r + r_{die})^2}{2h} + \frac{h}{2} - r_{die} \quad (18)$$

687 Equation (18) leads to good agreements with experimental values for dome
 688 heights, normalized by the diameter of the cavity, of up to $h/r = 0.56$ (see
 689 further details in [Gutscher et al. \(2004\)](#)). The same observation was made
 690 by [Liu et al. \(2015\)](#) for an AA7075 at elevated temperatures. Therefore,
 691 equation (18) was the one adopted in this work and used to calculate the
 692 biaxial stress using equation (12).

693 Regarding analytical methods for the evaluation of the thickness evolu-
 694 tion, [Hill \(1950\)](#) proposed the following relation:

$$t_{Hill} = t_0 \left(\frac{1}{1 + (h/r)^2} \right)^2 \quad (19)$$

695 Other authors, as [Reis et al. \(2016\)](#) have shown that the thickness evolution is
 696 also a function of other geometric parameters, as well as the work hardening
 697 coefficient and the orthotropic behaviour of the material. In this context,
 698 [Min et al. \(2017\)](#) proposed a method to calculate the effective stress at the
 699 specimen pole that takes into account the ratio of specimen thickness to
 700 the radius of curvature on the specimen outer surface, non-balanced biaxial
 701 curvatures in principal directions, the elastic deformation and bending effects.

702 Nevertheless, equation (19) is the one used in this work to evaluate the
 703 biaxial stress σ_b , with equation (12), and the bulge strain ε_b , with equation
 704 (16). Note that the height is the variable used to calculate the thickness and,
 705 consequently, to deduct the strain. Thus, the thermal strain is assumed to be

706 the strain resulting from the height reached by the pole before the expansion
707 starts (see equation 15).

708 The laser profilometer is placed 240 mm above the blank (see Figure 12),
709 *i.e.* above the copper bars feeding the electrodes of the device shown in Figure
710 6. A 3D printed adjustable mount assembly is used as shown in Figure 12-a.
711 The line observed by the profilometer is aligned with the rolling direction
712 of the blank, as shown in Figure 12-b. The length selected for the observed
713 profile was 50 mm, centered around the center of the blank, to ensure that the
714 apex of the bulge is accurately captured. The profilometer has a functionality
715 to calculate the radius of curvature directly but this option was not used since
716 the method used by the KEYENCE controller is not available to the public.
717 Equation (18) was therefore preferred, since some examples available in the
718 literature, such as Liu et al. (2015) indicate that it provides satisfactory
719 results. Nevertheless, it should be mentioned that the differences observed
720 between these two methods are negligible.

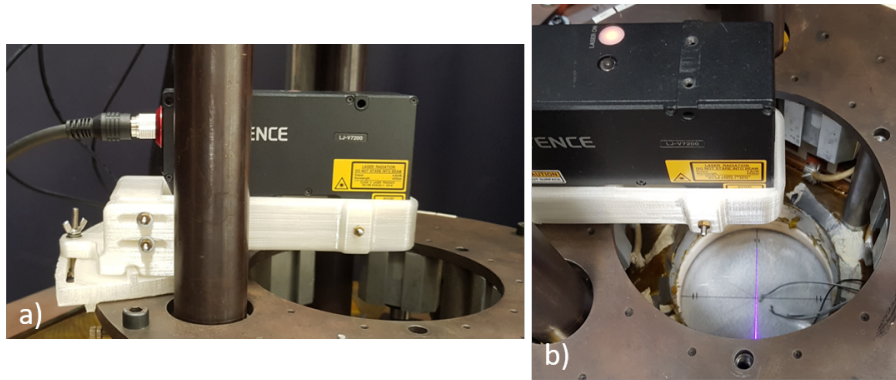


Figure 12: Mounting of the profilometer in the expansion device: a) Profile view of the 3D printed mount assembly; b) View of the laser on the blank's surface.

721 Before the test begins, *i.e.*, when the blank is at room temperature,
722 clamped and flat, a reference profile is saved with the controlling software
723 of the profilometer. From this reference profile, the height of the pole h is
724 deducted by taking the shortest distance between the highest point of the
725 current profile and the reference profile. The height of the pole is sampled
726 at 50 Hz.

727 To validate the use of the laser profilometer, bulge tests were performed
728 for an EN AW 6061-T6 aluminium alloy at 150 °C, which enables the appli-
729 cation of both measurement systems. The stress-strain curves were obtained
730 either with DIC or with the pole height evolution by the profilometer. The

731 procedure used the equations previously presented, including the thermal
 732 strain correction. Comparison using the laser-profilometer of the stress-strain
 733 curves obtained by DIC and profilometer methods, presented in a previous
 734 work by Boyer et al. (2019), showed a good agreement. This validation en-
 735 abled the application of the same method to analyse the expansion tests
 736 performed on boron steels, at high temperature.

737 4.2. Uniaxial tensile tests

738 Uniaxial tensile tests were performed with a Gleeble 3500 machine on
 739 Usibor[®]1500P steel. The specimen geometry is presented in Figure 13-a.
 740 The material used in these tests was sampled from a 0.9 mm thick sheet
 741 always with the length oriented along the rolling direction.

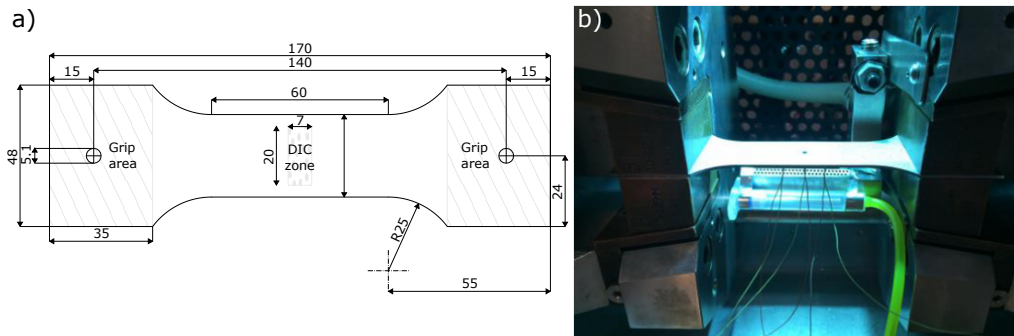


Figure 13: Uniaxial tensile test: a) Sample geometry; b) Test sample in the Gleeble 3500 machine.

742 A type *K* thermocouple, with a diameter of 250 μm was welded on the
 743 centre of the specimen by capacitive discharge, to control the temperature
 744 during the test, as detailed in Figure 13-b. The strain measurements were
 745 performed in a 7 by 20 mm^2 zone in the centre of the sample using the DIC
 746 system, GOM ARAMIS 4M. The selected dimensions were slightly lower
 747 than the gauge area in order to minimize the influence of border effects and
 748 of the non-uniform distribution of the temperature field. Two video cameras
 749 with a resolution of approximately 30 pixels mm^{-2} recorded the motion of
 750 the specimen surface at the maximum frequency of 50 Hz. The cameras
 751 of the DIC system were placed above the specimen gauge area, while the
 752 thermocouple was welded on its backside surface, as shown in Figure 13-b.
 753 It should be mentioned that the calibration of the DIC system is easier for the
 754 tensile test than for the expansion tests, due to the the smaller displacements
 755 that occur in the thickness direction, *i.e.* the distance between the specimen
 756 and the CCD cameras is kept constant.

757 *4.3. Experimental conditions reproducing the quenching*

758 Three temperatures of 900, 800 and 700 °C were chosen to reproduce the
 759 quenching conditions since they correspond to ones commonly used in the
 760 industry to perform forming operations. A schematic example of the temper-
 761 ature profile required to reproduce the quenching conditions at a prescribed
 762 temperature of 800 °C is presented in Figure 14. Figure 14-a shows the con-
 763 ditions for the tensile test while Figure 14-b corresponds to the bulge test.

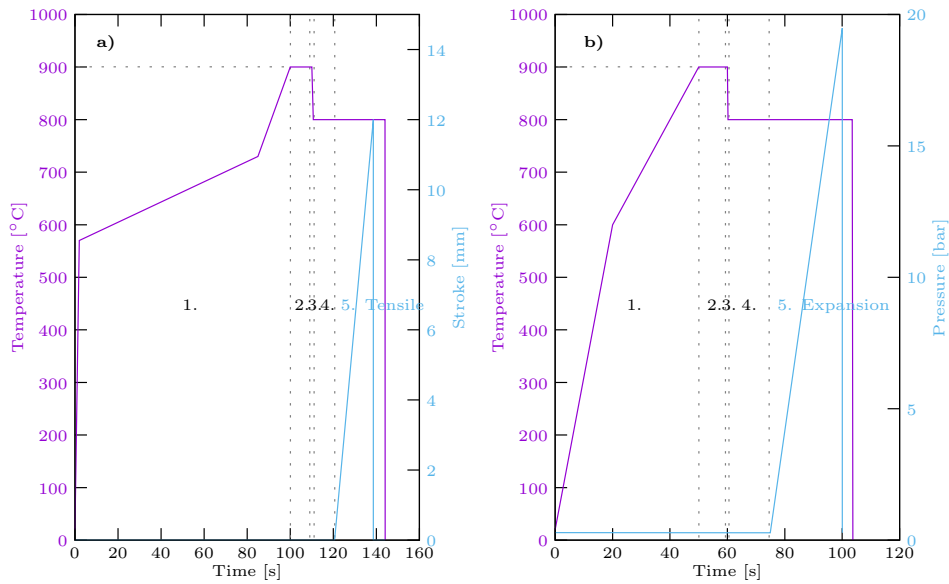


Figure 14: Schematic illustrating of the temperature profile and the loading condition during a) tensile and b) bulge tests, to obtain the stress-strain curves at temperature at 800 °C. Numbers indicate the different steps: 1. Heating; 2. Soaking; 3. Cooling; 4. Homogenization and 5. Loading.

764 For both expansion and tensile loading conditions, after a first heating,
 765 an austenitization (soaking) step is imposed, followed by a cooling step to
 766 attain the prescribed temperature. The cooling is controlled in the Gleeble
 767 machine with compressed air jet, while it is provided by natural convection
 768 and the heat conduction to the tools in the bulge test. Subsequently, an
 769 homogenization step is performed to stabilized the temperature across the
 770 blank. After this homogenization step, the pressure is linearly increased in
 771 the cavity as shown in Figure 14-b for the bulge test, while the displacement
 772 of grips is linearly increased for the tension test (see Figure 14-a), leading to
 773 an initial strain rate of 0.02 s^{-1} . Table 2 presents the durations of the different
 774 steps as well as the cooling-rate used in the bulge and uniaxial tensile tests.

| Conditions | 1. Heating | 2. Soaking | 3. Cooling | 4. Homogenisation | 5. Loading |
|------------|------------|------------|------------|-------------------|----------------------|
| Expansion | 50 s | 10 s | up to 12 s | 5 to 10 s | up to 50 s |
| Tensile | 100 s | 10 s | up to 2 s | 10 s | up to sample failure |

Table 2: Test cycle times for expansion and uniaxial tensile tests.

775 The main limitation of the bulge test device developed is that the tests
776 cannot last longer than 120s, to avoid the triggering of the thermal circuit
777 break. The bulging time is therefore limited by the time left available after
778 the heating, soaking, cooling and homogenization steps. Consequently, the
779 two pressure rates selected were 0.06 and 0.12 MPa s⁻¹.

780 By comparing Figures 14-a and 14-b, there are some differences in the
781 thermal cycles adopted for the expansion and uniaxial tests, particularly, dur-
782 ing the heating step. The heating time of the tensile tests is very high at the
783 beginning to avoid the degradation of the DIC pattern by controlling the to-
784 tal time of the test. This alternative is adopted since the heating rate around
785 the melting temperature of the coating is then drastically decrease to reduce
786 the current and so the Lorentz forces which induce the coating displacement.
787 This low heating rate avoids the displacement of the Al-Si coating during
788 its melting and therefore the decorrelation of the blank’s images during the
789 calculation of the deformations with the DIC system. Finally, the heating
790 rate between 730 to 900 °C is the same between tensile and bulge tests to
791 obtain the same microstructure (e.g. grain size) between the two types of
792 tests before the soaking step.

793 As mentioned in section 3.3, a soaking time between 2 and 10 s is sufficient
794 to form a fully martensitic structure. Therefore, a holding time of 10 s was
795 selected to assure the full austenization of the specimen both for tensile and
796 bulge tests.

797 As mentioned previously, the cooling rate in the bulge test is not con-
798 trolled, contrary to the tensile test where compressed air jets can be used to
799 quickly cool or quench. Thanks to these compressed air jets, the test tem-
800 perature is attained faster and more precisely during tensile tests. For the
801 bulge tests, the duration of the homogenization step varies between 5 to 10 s
802 due to difficulties to control the temperature during the cooling.

803 Furthermore, the lowest the temperature of the test, the longer the blank
804 will take to cool after the soaking period, limiting even more the bulging
805 time left. As a result of this constraint, the pressure rate of 0.06 MPa s⁻¹ is
806 the slowest that can be applied while assuring that a reasonable strain value
807 is attained, even for the lowest temperature studied of 700 °C. This is the
808 reason why the maximum strain values reached in the bulge tests vary with
809 the temperature and the pressure rate.

810 It is also important to mention that the control of the instant that the
811 cooling step should end is more difficult for lower values of the prescribed
812 temperature for the expansion tests. Note that the instructions for the control
813 must be prepared before the start of the test. The temperature attained
814 during the bulge step is conditioned by the PID and the error accumulated
815 during the heating step is compensated on the bulging step by the Integral
816 term of the PID (see also Figure 8). This compensation mechanism of
817 the PID regulation contributes to the difficulties encountered in tests repro-
818 ducibility. Four tests were successfully performed with a pressure rate of
819 0.12 MPa s^{-1} , for each temperature. For the 0.06 MPa s^{-1} pressure rate, only
820 two tests were performed for the 900 and 800 °C temperature, while only one
821 test was successfully performed at 700 °C. The test that shows a better evo-
822 lution of the prescribed temperature and pressure rate, for each condition,
823 is defined as the most representative for each test conditions and is the one
824 presented in this work.

825 This also explains why the expansion tests analysed in this study corre-
826 spond to blanks with different initial thickness, as presented in Table 3. The
827 first batch received presented a thickness of 0.9 mm while later batches with
828 1.0 mm were supplied. For 900 °C, the tests were performed with a thickness
829 of 0.9 mm. The tests at 800 °C correspond to a thickness of 1.0 mm. For
830 700 °C, the tests reported with the two pressure rates were performed with
831 different thicknesses. Only the blanks tested at 900 °C and the blank tested
832 at 800 °C with 0.12 MPa s^{-1} pressure rate reached the bursting pressure. For
833 the other temperatures and pressure rates, this is not achieved due to the
834 limitation imposed by the total time for the test. Table 3 summarizes the
835 initial blank thickness and if bursting was reached for each test performed.

| Test temperature (°C) | Parameters | 0.06 MPa s^{-1} | 0.12 MPa s^{-1} |
|-----------------------|------------|---------------------------|---------------------------|
| 900 | t_0 (mm) | 0.9 | 0.9 |
| | Burst | Yes | Yes |
| 800 | t_0 (mm) | 1.0 | 1.0 |
| | Burst | No | Yes |
| 700 | t_0 (mm) | 1.0 | 0.9 |
| | Burst | No | No |

Table 3: Bulge test blank initial thickness and bursting conditions at the end of the test for 700, 800 and 900 °C for 0.06 and 0.12 MPa s^{-1} pressure rates.

836 The uniaxial tensile tests were carried out using displacement control,
837 with a prescribed cross-head velocity to obtain the initial strain rate of
838 0.02 s^{-1} . Nevertheless, under these conditions, the strain rate can vary dur-

839 ing the test, since the length of the specimen is continuously increasing. On
840 the other hand, in the expansion tests, it is known that a constant pressure
841 rate does not lead to a constant strain rate.

842 The strain rate in each test was calculated by dividing the increment of
843 strain per the increment of time, using all consecutive data points available.
844 Nevertheless, it is known that the use of this forward difference to evalu-
845 ate the strain rate leads to some noise. This is particularly critical for the
846 expansion test, because the bulge strain is derived from the height of the
847 dome of the blank. The dome height measurement can be affected by the
848 profilometer sensor accuracy, which can result in oscillations on the height.
849 These oscillations can pollute the strain rate calculation and its subsequent
850 visualization. Smoothing techniques can be applied to prevent the apparition
851 of this phenomenon. In this study, for bulge test results, a sampling filter
852 was applied, considering one out of four data point available.

853 5. Results and discussion

854 The biaxial stress-strain curves for both pressure rates and three temper-
855 atures are presented in Figure 15-a. This figure presents also the stress-strain
856 curves for the uniaxial tensile tests for the three temperatures performed with
857 an initial strain rate of 0.02 s^{-1}

858 These evolutions are shown in function of the bulge stress and strain for
859 the expansion test and of the true stress and strain for tensile test. Note that
860 the direct comparison is possible when assuming that the material shows an
861 isotropic behaviour (see discussion in section 4.1.1). Dashed lines with crosses
862 are used to represent tensile tests whereas the continuous lines concerns bulge
863 tests results obtained with a pressure rate of 0.06 MPa s^{-1} and the ones for
864 0.12 MPa s^{-1} are represented with dashed lines.

865 Concerning tensile tests, although three tests were conducted for each
866 set of conditions, since the results show high reproducibility, only one was
867 selected to be presented in this figure. Moreover, the results are plotted only
868 up to the instant the maximal force is attained. Due to this condition, it
869 should be mentioned that the maximal strain range observed is within 0.10
870 at 900°C , 0.17 at 800°C and 0.096 at 700°C . Globally, the uniaxial tensile
871 tests show that the increase of temperature leads to an overall decrease of
872 the stress.

873 As previously mentioned, the difficulty to obtain a successful expansion
874 test with the lowest temperature and the 0.06 MPa s^{-1} pressure rate is high.
875 However, it should be mentioned that the bulge stress-strain results for the
876 0.12 MPa s^{-1} pressure rate show high reproducibility. Moreover, the evolu-
877 tion of the prescribed temperature and the pressure rate of the single test

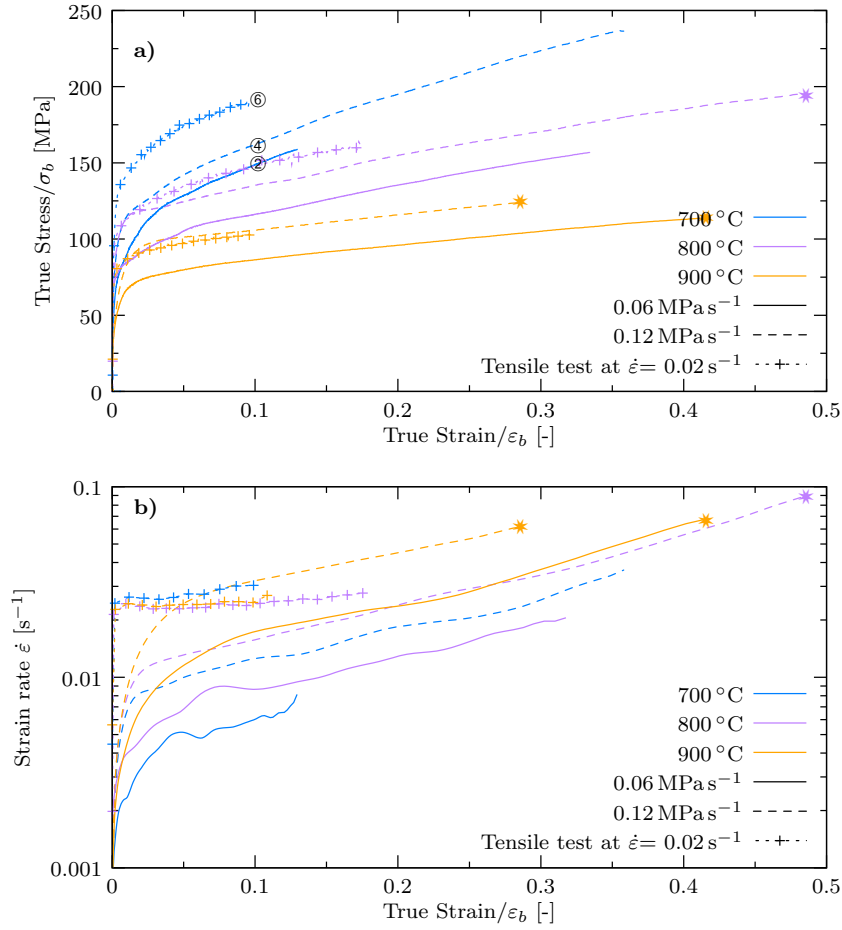


Figure 15: Expansion results at 700, 800 and 900 °C for 0.06 and 0.12 MPas⁻¹ pressure rates and comparison with uniaxial tensile tests for an initial strain rate of 0.02 s⁻¹; a) True Stress or σ_b versus True Strain or ε_b ; b) Strain rate versus True strain or ε_b . (*) indicates the burst of the specimen, the number indicates the instant the strain value of 0.096 is attained for ② 0.06 MPas⁻¹, ④ 0.12 MPas⁻¹ and ⑥ for tensile test, all performed at 700 °C).

878 performed at 0.06 MPas⁻¹ and 700 °C, gives confidence that it is representa-
 879 tive of the material's behaviour for those conditions.

880 The evolution of the strain rate during the expansion tests is presented
 881 in Figure 15-b. This figure presents also the strain rate evolution during
 882 the tensile test performed at a strain rate of 0.02 s⁻¹. The strain rate is
 883 almost constant for all the tensile tests, showing a slight increase at the end
 884 of the test. Unlike tensile tests, the strain rate during the expansion tests
 885 presents an increasing trend from the beginning. The linear increase of the

886 pressure in the cavity leads to a continuous increase of the strain rate over
887 the tests, regardless of the temperature or pressure rate. The strain rate
888 at the beginning of the test is 0.001 s^{-1} and afterwards increases fast, until
889 reaching a strain rate from which it starts to increase more slowly until the
890 end of the tests. These results show that the only strain rate for which it is
891 reasonable to make comparisons between both type of tests is the lowest one
892 used in the tensile test, *i.e.* 0.02 s^{-1} .

893 Only at $900\text{ }^{\circ}\text{C}$ the expansion tests were performed until burst. In this
894 case, the test at 0.12 MPa s^{-1} reaches a maximum strain value lower than
895 the one of the tests performed at 0.06 MPa s^{-1} , and both have deformations
896 larger than for tensile tests. The other tests were not performed up to the
897 blank failure, preventing any further discussion about the influence of the
898 strain rate on the formability.

899 Globally, the results from the expansion tests lead to conclusions similar
900 to the ones from tensile tests, in terms of thermal dependence. The hardening
901 evolution of the two expansion tests performed at the same temperature are
902 similar, with identical differences between the curves for the two pressure
903 rates, which indicate a positive strain rate sensitivity. However, Figure 15-
904 a shows that the evolution of the hardening slope of the expansion tests
905 presents non-negligible differences from the one obtained from uniaxial tensile
906 results.

907 At $900\text{ }^{\circ}\text{C}$, the yield strength is comparable between the expansion at
908 0.12 MPa s^{-1} and the tensile test. The tensile test stress is quite similar to
909 the one obtained with the higher pressure rate. Moreover, the expansion test
910 keeps a constant hardening slope although the strain rate keep increasing.
911 The relatively constant strain rate value of the tensile test is globally higher
912 than the one of the biaxial, which may explain the slightly higher initial yield
913 stress value attained for the tensile test.

914 At $800\text{ }^{\circ}\text{C}$, the yield strength of the tensile test is higher than the ones of
915 the expansion tests. For this temperature, the relatively constant strain rate
916 value of the tensile tests is globally higher than the one of the biaxial, which
917 may explain the slight higher stress value attained for the tensile test.

918 At $700\text{ }^{\circ}\text{C}$, the yield tensile stress is also higher than the one observed for
919 both expansion test. As for the other temperatures, this can be related with
920 the higher strain rate value attained in the tensile test, when compared with
921 the bulge tests. In fact, Figure 15-b shows that the differences in the strain
922 rate values between both type of tests are higher at lower temperatures. The
923 expansion tests performed at 0.12 MPa s^{-1} and 0.06 MPa s^{-1} show a similar
924 hardening trend, with a constant gap in the stress value, which seems to
925 correlate well with the difference in strain rate. Thus, although blank's with
926 different initial thickness were used that does not seem to affect the hardening

927 behaviour. Note that this direct comparison is possible when assuming that
928 the material shows an isotropic behaviour (see discussion in section 4.1.1) and
929 that the austenization step reduces the differences in the hardening behaviour
930 of rolled sheets with different thickness. It is also possible to note that the
931 strain rate evolution in expansion follows a linearly increasing trend, except
932 the test at 700 °C and 0.06 MPa s⁻¹, which never reaches the steady increasing
933 trend.

934 Although the main differences observed on the stress-strain curves be-
935 tween tensile and bulge tests at 700 °C can be explained based on the differ-
936 ent strain rate values, it is interesting to analyse the influence of the cooling
937 rate in the metallurgical transformations of the 22MnB5 steel. Figure 16
938 presents the Continuous Cooling Transformation (CCT) diagram of unde-
939 formed Usibor[®] 1500P presented in Ravier et al. (2003). This CCT diagram
940 shows the different phase transformations that can occur depending on the
941 cooling rate. Despite the durations of each step (heating, soaking and cool-
942 ing) are different from those of the tests performed in this study, it allows
943 to visualize the phase transformations that may occur during the uniaxial
944 tension and bulging tests.

945 It is also important to notice that during the cooling phase, the deforma-
946 tion of austenite has an influence on the transformation kinetics. Fan et al.
947 (2007) showed that this deformation of austenite may increase the ferrite nu-
948 cleation rate. In fact, a change in the austenitic content of the sample affects
949 the stress-strain response during the forming. Moreover, the prestrain is also
950 known to promote metallurgical transformations, as shown in Reitz et al.
951 (2022), with the shift of the A+F and A+B regions of the CCT diagram to
952 the left.

953 In Figure 16, the temperature evolution in function of time for the two
954 bulge tests performed at 700 °C are compared with the one of tensile test
955 performed at 700 °C, with an initial strain rate value of 0.02 s⁻¹. As shown
956 in Table 2, bulge and tensile tests were performed with different cooling rates,
957 which are also evident in Figure 16. Although the CCT diagram was obtained
958 for a different soaking time and cooling rate, it is possible to observe that the
959 higher cooling rate used in the uniaxial tensile tests is better suited to ensure
960 the material microstructure is fully austenitic, at the end of the test, even
961 when applying a smaller strain rate (tests with longer duration). According
962 to Figure 16, the smaller cooling rate attained with the bulge test device
963 can promote the formation of ferrite in the microstructure. This may also
964 contribute to some differences in the hardening behaviour between tensile
965 and expansion tests at 700 °C. A better control of the cooling performance
966 of the expansion device would allow a better prediction of the time required
967 to reach the test temperature. Thus, it would allow to trigger the expansion

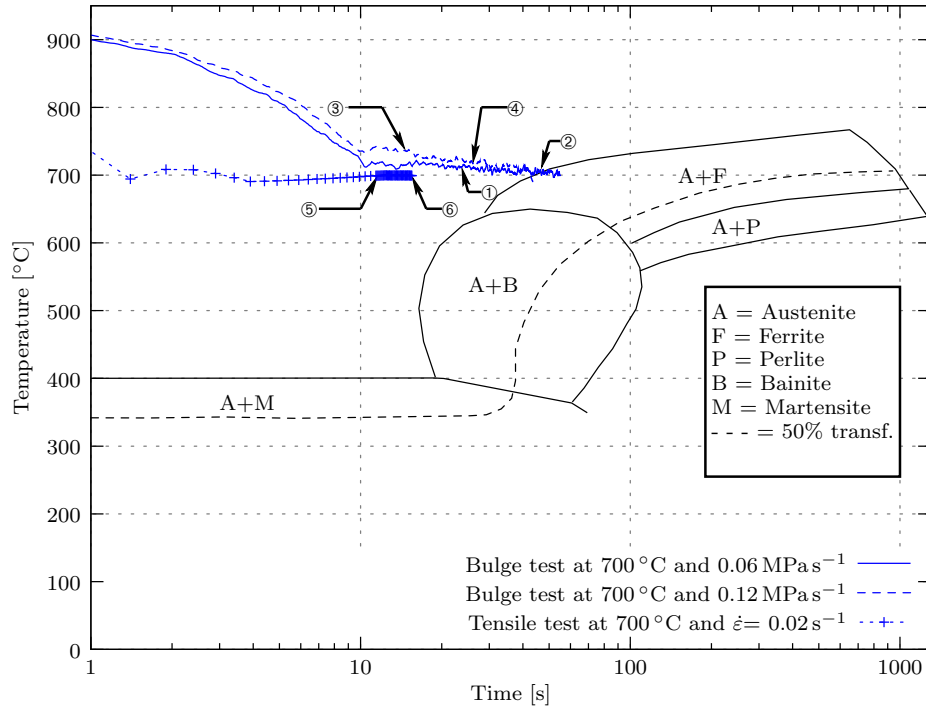


Figure 16: Continuous Cooling Transformation diagram from Ravier et al. (2003) with the evolution of the temperature *versus* time for the bulge test at 700 °C for 0.06 and 0.12 MPas⁻¹ pressure rates and uniaxial tensile test with an initial strain rate value of 0.02 s⁻¹ (the odd numbers indicate the start of the forming stage: ① 0.06 MPas⁻¹, ③ 0.12 MPas⁻¹ and ⑤ for tensile test; the even numbers indicate the instant the strain value of 0.096 is attained for: ② 0.06 MPas⁻¹, ④ 0.12 MPas⁻¹ and ⑥ for tensile test).

968 phase sooner, reducing the possibility of microstructural changes in the blank
 969 during the expansion phase.

970 6. Conclusion

971 This work addresses one of the major challenges in the acquisition of
 972 the biaxial stress-strain curve from the hydraulic bulge test at high tem-
 973 perature: ensuring a homogeneous temperature field on the dome area. To
 974 overcome this problem, an innovative procedure, based on the heating Joule
 975 effect, was designed with the aid of a multi-physic model using COMSOL
 976 Multiphysics[®]. This heating method was selected since the aim is to uni-
 977 formly heat and austenize complex shape blanks of Usibor[®]1500P steel in
 978 conditions that resemble the ones used on hot forming processes (i.e. consid-
 979 ering short heating and soaking times for an austenitization temperature of

980 900 °C). The heating method developed allows not only imposing a uniform
981 temperature in the dome area, but also maintaining it during the bulging.

982 A new hydraulic bulge test device at high temperature was implemented
983 showing good correlation with the numerical model and demonstrating its
984 capability to reproduce accurately the temperature cycle of hot forming.
985 Nevertheless, the short time to calibrate the DIC system at high tempera-
986 ture, combined with the degradation of the pattern (amplified by the biaxial
987 deformation) and by the presence of the Al-Si coating, resulted in the in-
988 ability to apply DIC techniques to measure the principle strains during the
989 process and, consequently, the curvature and the thickness evolutions. These
990 difficulties are carefully detailed since this is other of the major challenges in
991 the acquisition of the biaxial stress-strain curve from the hydraulic bulge test
992 at high temperature. To circumvent this limitation, a compromise alternative
993 was adopted that uses a laser profilometer. This means that the curvature
994 and thickness are determined using analytical expressions that relate their
995 evolutions with the pole height.

996 The mechanical behaviour of the Usibor[®]1500P steel was also evaluated
997 in uniaxial tensile conditions on a Gleeble machine with a DIC system and
998 the results were compared with the ones obtained using the new expansion
999 device for three different temperatures. Uniaxial tensile tests were performed
1000 for a single strain rate value while two pressure rate values were selected for
1001 the bulge tests. The constant pressure rate of the bulge test resulted in a
1002 continuous increase of the strain rate during the tests. The uniaxial tensile
1003 tests show that the increase of temperature leads to an overall decrease of
1004 the stress. The bulge test results also capture the decrease of stress with
1005 temperature and highlight the positive strain rate sensitivity.

1006 Nevertheless, the constant pressure rate applied during the bulge test re-
1007 sults in a continuous increase of the strain rate during the tests. The control
1008 of the strain-rate is very difficult because it requires the acquisition of the
1009 thickness strain, continuously during the test. This is another major chal-
1010 lenge in the acquisition of the biaxial stress-strain curve from the hydraulic
1011 bulge test at high temperature, which was not tackled in this work. De-
1012 spite the difficulties reported in this study for the Usibor[®]1500P steel, the
1013 new hydraulic bulge test device enables a fast heating of the specimens to
1014 hot temperature conditions, assuring a homogeneous temperature field in the
1015 dome while enabling the acquisition of the principle strains through DIC, as
1016 previously reported for an aluminium alloy by [Boyer et al. \(2019\)](#).

1017 Acknowledgements

1018 This work was part of the ANR PRICECAT project, which is sup-
1019 ported by the National Agency of Research (ANR) under the ANR-13-
1020 RMNP-0009-03. This research was also supported by the French Ministry of
1021 Higher Education and the Portuguese Foundation for Science and Technol-
1022 ogy (FCT) via the projects PTDC/EME-EME/30592/2017 (POCI-01-0145-
1023 FEDER-030592), PTDC/EME-APL/29713/2017 (POCI-01-0145-FEDER-
1024 029713), UIDB/00285/2020 and LA/P/0112/2020. The authors would like
1025 to thank the society SREM Technologies-France (<http://www.srem.fr/fr/>),
1026 for the design and conception of the device and for the furniture of the elec-
1027 trical generator. They also gratefully acknowledge research support from R.
1028 Canivenc, J. Favero, H. Salmon-Legagneur and G. Brun from ArcelorMittal
1029 (Montataire-France) and the technical support provided by A. Jegat (IRDL)
1030 during the experimental campaigns.

1031 References

- 1032 Abu-Farha, F., Hector, L.G., 2011. Sheet Orientation Effects on the Hot
1033 Formability Limits of Lightweight Alloys. *Journal of Manufacturing Sci-*
1034 *ence and Engineering* 133, 061005–061005. doi:[10.1115/1.4004850](https://doi.org/10.1115/1.4004850).
- 1035 Aksenov, S., Sorgente, D., 2020. Determination of biaxial stress–strain curves
1036 for superplastic materials by means of bulge forming tests at constant
1037 stress. *CIRP Journal of Manufacturing Science and Technology* 31, 618–
1038 627. doi:[10.1016/j.cirpj.2020.09.002](https://doi.org/10.1016/j.cirpj.2020.09.002).
- 1039 Alharthi, H., Hazra, S., Alghamdi, A., Banabic, D., Dashwood, R., 2018.
1040 Determination of the yield loci of four sheet materials (AA6111-T4, AC600,
1041 DX54d+Z, and H220bd+Z) by using uniaxial tensile and hydraulic bulge
1042 tests. *Int J Adv Manuf Technol* doi:[10.1007/s00170-018-2339-5](https://doi.org/10.1007/s00170-018-2339-5).
- 1043 Ayres, R.A., Wenner, M.L., 1979. Strain and strain-rate hardening effects in
1044 punch stretching of 5182-0 aluminum at elevated temperatures. *MTA* 10,
1045 41–46. doi:[10.1007/BF02686404](https://doi.org/10.1007/BF02686404).
- 1046 Banabic, D., Vulcan, M., Siegert, K., 2005. Bulge Testing under Constant
1047 and Variable Strain Rates of Superplastic Aluminium Alloys. *CIRP Annals*
1048 54, 205–208. doi:[10.1016/S0007-8506\(07\)60084-5](https://doi.org/10.1016/S0007-8506(07)60084-5).
- 1049 Bariani, P.F., Bruschi, S., Ghiotti, A., Turetta, A., 2008. Testing formability
1050 in the hot stamping of HSS. *CIRP Annals - Manufacturing Technology*
1051 57, 265–268. doi:[10.1016/j.cirp.2008.03.049](https://doi.org/10.1016/j.cirp.2008.03.049).

- 1052 Behrens, B., Hübner, S., Schrodter, J., Uhe, J., 2015. Conductive heating
1053 opens up various new opportunities in hot stamping, in: Proceedings of
1054 5Th International Conference on Accuracy in Forming, Toronto. pp. 157–
1055 173.
- 1056 Blaise, A., Bourouga, B., Abdulhay, B., Dessain, C., 2013. Thermal con-
1057 tact resistance estimation and metallurgical transformation identification
1058 during the hot stamping. Applied Thermal Engineering 61, 141–148.
1059 doi:[10.1016/j.applthermaleng.2013.07.041](https://doi.org/10.1016/j.applthermaleng.2013.07.041).
- 1060 Bleck, W., Blumbach, M., 2005. Laser-Aided Flow Curve Determination in
1061 Hydraulic Bulging. Steel research international 76, 125–130. doi:[10.1002/
1062 srin.200505983](https://doi.org/10.1002/srin.200505983).
- 1063 Boudeau, N., Vitu, L., Laforge, N., Malécot, P., Michel, G., Milesi, M.,
1064 Manov, S., 2018. How to Post-Process Experimental Results from the
1065 Flange Bulging Test? Application to the characterization of a Zinc alloy.
1066 IOP Conference Series: Materials Science and Engineering 418, 012086.
1067 doi:[10.1088/1757-899X/418/1/012086](https://doi.org/10.1088/1757-899X/418/1/012086).
- 1068 Boyer, A., Laurent, H., Oliveira, M.C., 2019. Evaluation of the stress vs strain
1069 curve using a high temperature bulge test device. IOP Conference Series:
1070 Materials Science and Engineering 651, 012048. doi:[10.1088/1757-899X/
1071 651/1/012048](https://doi.org/10.1088/1757-899X/651/1/012048).
- 1072 Braun, A., Bambach, M., Hirt, G., 2014a. Investigation of a Bulge Test at
1073 High Temperatures and High Strain Rates Using a Finite-Element Simu-
1074 lation Study. Key Engineering Materials 622-623, 300–307. doi:[10.4028/
1075 www.scientific.net/KEM.622-623.300](https://doi.org/10.4028/www.scientific.net/KEM.622-623.300).
- 1076 Braun, A., Storz, J., Bambach, M., Hirt, G., 2014b. Development of a Pneu-
1077 matic Bulge Test for High Temperatures and Controlled Strain Rates. Ad-
1078 vanced Materials Research 1018, 245–252. doi:[10.4028/www.scientific.
1079 net/AMR.1018.245](https://doi.org/10.4028/www.scientific.net/AMR.1018.245).
- 1080 Braun, A., Waerder, M., Hirt, G., 2016. Forming limit and Flow curve de-
1081 termination of hot stamping steels using a hot-gas-bulge-test, in: Forming
1082 Technology Forum 2016, Munich.
- 1083 Chen, K., Scales, M., Kyriakides, S., Corona, E., 2016. Effects of anisotropy
1084 on material hardening and burst in the bulge test. International Journal of
1085 Solids and Structures 82, 70 – 84. doi:[10.1016/j.ijsolstr.2015.12.012](https://doi.org/10.1016/j.ijsolstr.2015.12.012).

- 1086 Demazel, N., 2018. Développement d'une solution de chauffage par con-
1087 duction électrique pour l'emboutissage des aciers trempants : approche
1088 numérique et expérimentale. Ph.D. thesis. Université Bretagne Sud. URL:
1089 <http://www.theses.fr/s131042>.
- 1090 Demazel, N., Carin, M., Laurent, H., Le Masson, P.L., Coër, J., Favero, J.,
1091 Canivenc, R., Glock, F., Graveleau, S., 2016. Numerical optimization of
1092 Joule heating process of Usibor[®]1500 automotive blanks, in: NUMIFORM
1093 2016, p. 3. URL: <http://numiform2016.utt.fr/Papers/91.pdf>.
- 1094 Demazel, N., Laurent, H., Carin, M., Le Masson, P., Salmon-Legagneur, H.,
1095 2021. A direct resistance heating method for shaped blank. Journal of
1096 Manufacturing Processes 62, 772–783. doi:[10.1016/j.jmapro.2020.12.](https://doi.org/10.1016/j.jmapro.2020.12.056)
1097 [056](https://doi.org/10.1016/j.jmapro.2020.12.056).
- 1098 Demazel, N., Laurent, H., Coër, J., Carin, M., Masson, P.L., Favero, J.,
1099 Canivenc, R., Salmon-Legagneur, H., 2018. Investigation of the progressive
1100 hot die stamping of a complex boron steel part using numerical simulations
1101 and Gleeble tests. The International Journal of Advanced Manufacturing
1102 Technology , 1–15doi:[10.1007/s00170-018-2532-6](https://doi.org/10.1007/s00170-018-2532-6).
- 1103 Deng, T., Li, D., Li, X., 2018. Temperature variation model of titanium
1104 alloy L-angle profile in hot stretch forming with resistance heating. The
1105 International Journal of Advanced Manufacturing Technology 95, 2105–
1106 2110. doi:[10.1007/s00170-017-1334-6](https://doi.org/10.1007/s00170-017-1334-6).
- 1107 Dutta, A., Mukherjee, A.K., 1992. Superplastic forming: an analytical ap-
1108 proach. Materials Science and Engineering: A 157, 9–13. doi:[10.1016/
1109 0921-5093\(92\)90092-F](https://doi.org/10.1016/0921-5093(92)90092-F).
- 1110 Fan, D., Kim, H., Biroasca, S., De Cooman, B.C., 2007. Critical review of hot
1111 stamping technology for automotive steels, in: Proceedings from the Ma-
1112 terials Science & Technology Conference MS&T 2007, Detroit, Michigan,
1113 USA. pp. 98–109.
- 1114 Groche, P., Huber, R., Dörr, J., Schmoeckel, D., 2002. Hydrome-
1115 chanical Deep-Drawing of Aluminium-Alloys at Elevated Temperatures.
1116 CIRP Annals - Manufacturing Technology 51, 215–218. doi:[10.1016/
1117 S0007-8506\(07\)61502-9](https://doi.org/10.1016/S0007-8506(07)61502-9).
- 1118 Gutscher, G., Wu, H.C., Ngaile, G., Altan, T., 2004. Determination of flow
1119 stress for sheet metal forming using the viscous pressure bulge (VPB)
1120 test. Journal of Materials Processing Technology 146, 1–7. doi:[10.1016/
1121 S0924-0136\(03\)00838-0](https://doi.org/10.1016/S0924-0136(03)00838-0).

- 1122 Hill, R., 1950. A theory of the plastic bulging of a metal diaphragm by lateral
1123 pressure. *Philosophical Magazine and Journal of Science* 41, 1133–1142.
1124 doi:[10.1080/14786445008561154](https://doi.org/10.1080/14786445008561154).
- 1125 Hou, Z., Min, J., Wang, J., Lu, Q., He, Z., Chai, Z., Xu, W., 2021. Effect
1126 of Rapid Heating on Microstructure and Tensile Properties of a Novel
1127 Coating-Free Oxidation-Resistant Press-Hardening Steel. *JOM* 73, 3195–
1128 3203. doi:[10.1007/s11837-021-04877-7](https://doi.org/10.1007/s11837-021-04877-7).
- 1129 ISO16808, 2014. Metallic materials – Sheet and strip – Determination of
1130 biaxial stress-strain curve by means of bulge test with optical measuring
1131 systems. URL: <https://www.iso.org/standard/57777.html>.
- 1132 Jocham, D., Norz, R., Volk, W., 2017. Strain rate sensitivity of DC06 for
1133 high strains under biaxial stress in hydraulic bulge test and under uniaxial
1134 stress in tensile test. *International Journal of Material Forming* 10, 453–
1135 461. doi:[10.1007/s12289-016-1293-8](https://doi.org/10.1007/s12289-016-1293-8).
- 1136 Jovane, F., 1968. An approximate analysis of the superplastic forming of a
1137 thin circular diaphragm: Theory and experiments. *International Journal of*
1138 *Mechanical Sciences* 10, 403–427. doi:[10.1016/0020-7403\(68\)90005-2](https://doi.org/10.1016/0020-7403(68)90005-2).
- 1139 Karbasian, H., Tekkaya, A., 2010. A review on hot stamping. *Journal of*
1140 *Materials Processing Technology* 210, 2103–2118. doi:[10.1016/j.jmatprotec.2010.07.019](https://doi.org/10.1016/j.jmatprotec.2010.07.019).
- 1142 Kaya, S., Altan, T., Groche, P., Klöpsch, C., 2008. Determination of the
1143 flow stress of magnesium AZ31-O sheet at elevated temperatures using the
1144 hydraulic bulge test. *International Journal of Machine Tools and Manu-*
1145 *facture* 48, 550–557. doi:[10.1016/j.ijmachtools.2007.06.011](https://doi.org/10.1016/j.ijmachtools.2007.06.011).
- 1146 Koç, M., Billur, E., Cora, O.N., 2011. An experimental study on the com-
1147 parative assessment of hydraulic bulge test analysis methods. *Materials &*
1148 *Design* 32, 272 – 281. doi:[10.1016/j.matdes.2010.05.057](https://doi.org/10.1016/j.matdes.2010.05.057).
- 1149 Kolleck, R., Veit, R., Hofmann, H., Lenze, F., 2008. Alternative heating
1150 concepts for hot sheet metal forming, in: 1st International Conference on
1151 Hot Sheet Metal Forming of High-Performance Steel, pp. 239–246.
- 1152 Kolleck, R., Veit, R., Merklein, M., Lechler, J., Geiger, M., 2009. Investiga-
1153 tion on induction heating for hot stamping of boron alloyed steels. *CIRP*
1154 *Annals* 58, 275–278. doi:[10.1016/j.cirp.2009.03.090](https://doi.org/10.1016/j.cirp.2009.03.090).

- 1155 Lafilé, V., Galpin, B., Mahéo, L., Roth, C.C., Grolleau, V., 2021. Toward the
1156 use of small size bulge tests: Numerical and experimental study at small
1157 bulge diameter to sheet thickness ratios. *Journal of Materials Processing*
1158 *Technology* 291, 117019. doi:[10.1016/j.jmatprotec.2020.117019](https://doi.org/10.1016/j.jmatprotec.2020.117019).
- 1159 Lee, J.Y., Xu, L., Barlat, F., Wagoner, R.H., Lee, M.G., 2013. Balanced Bi-
1160 axial Testing of Advanced High Strength Steels in Warm Conditions. *Ex-*
1161 *perimental Mechanics* 53, 1681–1692. doi:[10.1007/s11340-013-9758-x](https://doi.org/10.1007/s11340-013-9758-x).
- 1162 Li, C., Jiang, S., Zhang, K., 2012. Pulse current-assisted hot-forming of
1163 light metal alloy. *Int J Adv Manuf Technol* 63, 931–938. doi:[10.1007/
1164 s00170-012-3934-5](https://doi.org/10.1007/s00170-012-3934-5).
- 1165 Li, D., Ghosh, A.K., 2004. Biaxial warm forming behavior of aluminum
1166 sheet alloys. *Journal of Materials Processing Technology* 145, 281–293.
1167 doi:[10.1016/j.jmatprotec.2003.07.003](https://doi.org/10.1016/j.jmatprotec.2003.07.003).
- 1168 Li, Y., Li, S., Chen, Y., Han, G., 2019. Constitutive parameters identification
1169 based on DIC assisted thermo-mechanical tensile test for hot stamping of
1170 boron steel. *Journal of Materials Processing Technology* 271, 429–443.
1171 doi:[10.1016/j.jmatprotec.2019.04.020](https://doi.org/10.1016/j.jmatprotec.2019.04.020).
- 1172 Liang, W., Wang, H., Wang, Q., Liu, Q., Zhang, Y., 2021. Application of
1173 conduction heating on hot stamping of front bumper. *The International*
1174 *Journal of Advanced Manufacturing Technology* 112, 3177–3188. doi:[10.
1175 1007/s00170-021-06618-1](https://doi.org/10.1007/s00170-021-06618-1).
- 1176 Liang, W.K., Wang, L., Liu, Y., Wang, Y.L., Zhang, Y.S., 2014. Blank
1177 Shape Sensitivity on Temperature Distribution of Hot Stamping Boron
1178 Steel through Conduction Heating. *Advanced Materials Research* 1063,
1179 211–214. doi:[10.4028/www.scientific.net/AMR.1063.211](https://doi.org/10.4028/www.scientific.net/AMR.1063.211).
- 1180 Liu, K., Lang, L., Cai, G., Yang, X., Guo, C., Liu, B., 2015. A novel approach
1181 to determine plastic hardening curves of AA7075 sheet utilizing hydraulic
1182 bulging test at elevated temperature. *International Journal of Mechanical*
1183 *Sciences* 100, 328–338. doi:[10.1016/j.ijmecsci.2015.07.002](https://doi.org/10.1016/j.ijmecsci.2015.07.002).
- 1184 Loulou, T., Masson, P.L., Rogeon, P., 2006. Thermal characteri-
1185 zation of resistance spot welding. *Numerical Heat Transfer, Part*
1186 *B: Fundamentals* 49, 559–584. doi:[10.1080/10407790500433986](https://doi.org/10.1080/10407790500433986),
1187 [arXiv:http://dx.doi.org/10.1080/10407790500433986](https://arxiv.org/http://dx.doi.org/10.1080/10407790500433986).

- 1188 Lăzărescu, L., Comşa, D.S., Banabic, D., 2011. Determination of Stress-
1189 Strain Curves of Sheet Metals by Hydraulic Bulge Test, in: AIP Conference
1190 Proceedings, AIP Publishing. pp. 1429–1434. doi:[10.1063/1.3589717](https://doi.org/10.1063/1.3589717).
- 1191 Löbbe, C., Hering, O., Hiegemann, L., Tekkaya, A.E., 2016. Setting me-
1192 chanical properties of high strength steels for rapid hot forming processes.
1193 Materials 9. doi:[10.3390/ma9040229](https://doi.org/10.3390/ma9040229).
- 1194 Machado, G., Favier, D., Chagnon, G., 2012. Membrane Curvatures and
1195 Stress-strain Full Fields of Axisymmetric Bulge Tests from 3d-DIC Mea-
1196 surements. Theory and Validation on Virtual and Experimental results.
1197 Experimental Mechanics 52, 865–880. doi:[10.1007/s11340-011-9571-3](https://doi.org/10.1007/s11340-011-9571-3).
- 1198 Maeno, T., Mori, K.i., Ogihara, T., Fujita, T., 2018. Blanking immediately
1199 after heating and ultrasonic cleaning for compact hot-stamping systems
1200 using rapid resistance heating. Int J Adv Manuf Technol 97, 3827–3837.
1201 doi:[10.1007/s00170-018-2232-2](https://doi.org/10.1007/s00170-018-2232-2).
- 1202 Maeno, T., Mori, K.i., Ogihara, T., Fujita, T., 2019. Removal of thin oxide
1203 scale by ultrasonic cleaning with diluted hydrochloric acid in hot stamping
1204 of bare 22MnB5 sheet using resistance heating. Procedia Manufacturing
1205 29, 225–231. doi:[10.1016/j.promfg.2019.02.130](https://doi.org/10.1016/j.promfg.2019.02.130).
- 1206 Maeno, T., Mori, K.i., Sakagami, M., Nakao, Y., Talebi-Anaraki, A., 2020.
1207 Minimisation of heating time for full hardening in hot stamping using direct
1208 resistance heating. Journal of Manufacturing and Materials Processing 4.
1209 doi:[10.3390/jmmp4030080](https://doi.org/10.3390/jmmp4030080).
- 1210 Mahabunphachai, S., Koç, M., 2010. Investigations on forming of aluminum
1211 5052 and 6061 sheet alloys at warm temperatures. Materials & Design 31,
1212 2422–2434. doi:[10.1016/j.matdes.2009.11.053](https://doi.org/10.1016/j.matdes.2009.11.053).
- 1213 Merklein, M., Lecher, J., Gödel, V., Bruschi, S., Ghiotti, A., Turetta, A.,
1214 2007. Mechanical properties and plastic anisotropy of the quenchenable
1215 high strength steel 22mnb5 at elevated temperatures, in: Sheet Metal 2007,
1216 Trans Tech Publications Ltd. pp. 79–86. doi:[10.4028/www.scientific.net/KEM.344.79](https://doi.org/10.4028/www.scientific.net/KEM.344.79).
- 1218 Merklein, M., Lechler, J., 2006. Investigation of the thermo-mechanical prop-
1219 erties of hot stamping steels. Journal of Materials Processing Technology
1220 177, 452–455. doi:[10.1016/j.jmatprotec.2006.03.233](https://doi.org/10.1016/j.jmatprotec.2006.03.233).
- 1221 Min, J., Stoughton, T.B., Carsley, J.E., Carlson, B.E., Lin, J., Gao, X.,
1222 2017. Accurate characterization of biaxial stress-strain response of sheet

- 1223 metal from bulge testing. *International Journal of Plasticity* 94, 192–213.
1224 doi:[10.1016/j.ijplas.2016.02.005](https://doi.org/10.1016/j.ijplas.2016.02.005).
- 1225 Mori, K., Bariani, P.F., Behrens, B.A., Brosius, A., Bruschi, S., Maeno, T.,
1226 Merklein, M., Yanagimoto, J., 2017. Hot stamping of ultra-high strength
1227 steel parts. *CIRP Annals* 66, 755–777. doi:[10.1016/j.cirp.2017.05.007](https://doi.org/10.1016/j.cirp.2017.05.007).
- 1228 Mori, K., Maki, S., Tanaka, Y., 2005. Warm and Hot Stamping of Ultra High
1229 Tensile Strength Steel Sheets Using Resistance Heating. *CIRP Annals* 54,
1230 209–212. doi:[10.1016/S0007-8506\(07\)60085-7](https://doi.org/10.1016/S0007-8506(07)60085-7).
- 1231 Mori, K.i., Abe, Y., Miyazawa, S., 2020. Warm stamping of ultra-high
1232 strength steel sheets at comparatively low temperatures using rapid re-
1233 sistance heating. *The International Journal of Advanced Manufacturing*
1234 *Technology* 108, 3885–3891. doi:[10.1007/s00170-020-05642-x](https://doi.org/10.1007/s00170-020-05642-x).
- 1235 Mulder, J., Vegter, H., Aretz, H., Keller, S., van den Boogaard, A.H., 2015.
1236 Accurate determination of flow curves using the bulge test with optical
1237 measuring systems. *Journal of Materials Processing Technology* 226, 169–
1238 187. doi:[10.1016/j.jmatprotec.2015.06.034](https://doi.org/10.1016/j.jmatprotec.2015.06.034).
- 1239 Nakagawa, Y., ichiro Mori, K., Nishikata, M., 2020. Hot stamping of non-
1240 rectangular steel sheets using resistance heating by local preheating. *Pro-*
1241 *cedia Manufacturing* 50, 298–302. doi:[10.1016/j.promfg.2020.08.055](https://doi.org/10.1016/j.promfg.2020.08.055).
1242 18th International Conference on Metal Forming 2020.
- 1243 Panknin, W., 1959. Der hydraulische Tiefungsversuch und die Ermittlung
1244 von Fließkurven (The hydraulic bulge test and the determination of the
1245 flow stress curves). Ph.D. thesis. University of Stuttgart.
- 1246 Pradille, C., Bay, F., Mocellin, K., 2010. An Experimental Study to De-
1247 termine Electrical Contact Resistance, in: 2010 Proceedings of the 56th
1248 IEEE Holm Conference on Electrical Contacts, pp. 1–5. doi:[10.1109/
1249 HOLM.2010.5619522](https://doi.org/10.1109/HOLM.2010.5619522).
- 1250 Ravier, P., Aranda, L.G., Chastel, Y., 2003. Hot Stamping Experiment And
1251 Numerical Simulation Of Pre-coated USIBOR1500 Quenchable Steels, pp.
1252 2003–01–2859. doi:[10.4271/2003-01-2859](https://doi.org/10.4271/2003-01-2859).
- 1253 Reis, L.C., Oliveira, M.C., Santos, A.D., Fernandes, J.V., 2016. On the de-
1254 termination of the work hardening curve using the bulge test. *International*
1255 *Journal of Mechanical Sciences* 105, 158–181. doi:[10.1016/j.ijmecsci.
1256 2015.11.009](https://doi.org/10.1016/j.ijmecsci.2015.11.009).

- 1257 Reitz, A., Grydin, O., Schaper, M., 2022. Influence of thermomechanical pro-
1258 cessing on the microstructural and mechanical properties of steel 22MnB5.
1259 Materials Science and Engineering: A 838, 142780. doi:[doi.org/10.1016/
1260 j.msea.2022.142780](https://doi.org/10.1016/j.msea.2022.142780).
- 1261 Rogeon, P., Raelison, R., Carre, P., Dechalotte, F., 2008. A Micro-
1262 scopic Approach to Determine Electrothermal Contact Conditions Dur-
1263 ing Resistance Spot Welding Process. Journal of Heat Transfer 131.
1264 doi:[10.1115/1.3000596](https://doi.org/10.1115/1.3000596).
- 1265 Santos, T.G., Miranda, R.M., Vilaça, P., 2014. Friction Stir Welding Assisted
1266 by Electrical Joule Effect. Journal of Materials Processing Technology
1267 doi:[10.1016/j.jmatprotec.2014.03.012](https://doi.org/10.1016/j.jmatprotec.2014.03.012).
- 1268 Sène, N.A., Balland, P., Arrieux, R., Bouabdallah, K., 2013. An Experimen-
1269 tal Study of the Microformability of Very Thin Materials. Experimental
1270 Mechanics 53, 155–162. doi:[10.1007/s11340-012-9623-3](https://doi.org/10.1007/s11340-012-9623-3).
- 1271 Shao, Z., Bai, Q., Li, N., Lin, J., Shi, Z., Stanton, M., Watson, D., Dean,
1272 T., 2018. Experimental investigation of forming limit curves and defor-
1273 mation features in warm forming of an aluminium alloy. Proceedings of
1274 the Institution of Mechanical Engineers, Part B: Journal of Engineering
1275 Manufacture 232, 465–474. doi:[10.1177/0954405416645776](https://doi.org/10.1177/0954405416645776).
- 1276 Shao, Z., Li, N., Lin, J., Dean, T.A., 2016. Development of a New Biaxial
1277 Testing System for Generating Forming Limit Diagrams for Sheet Metals
1278 Under Hot Stamping Conditions. Experimental Mechanics 56, 1489–1500.
1279 doi:[10.1007/s11340-016-0183-9](https://doi.org/10.1007/s11340-016-0183-9).
- 1280 Suttner, S., Merklein, M., 2016. Experimental and numerical investigation of
1281 a strain rate controlled hydraulic bulge test of sheet metal. Journal of Ma-
1282 terials Processing Technology 235, 121–133. doi:[10.1016/j.jmatprotec.
1283 2016.04.022](https://doi.org/10.1016/j.jmatprotec.2016.04.022).
- 1284 Terhorst, M., Ozhoga-Maslovskaja, O., Trauth, D., Shirobokov, A., Mattfeld,
1285 P., Solf, M., Klocke, F., 2016. Electro-thermo-mechanical contact model
1286 for bulk metal forming under application of electrical resistance heating.
1287 Int J Adv Manuf Technol , 1–18doi:[10.1007/s00170-016-9315-8](https://doi.org/10.1007/s00170-016-9315-8).
- 1288 Venturato, G., Novella, M., Bruschi, S., Ghiotti, A., Shivpuri, R., 2017. Ef-
1289 fects of Phase Transformation in Hot Stamping of 22MnB5 High Strength
1290 Steel. Procedia Engineering 183, 316–321. doi:[10.1016/j.proeng.2017.
1291 04.045](https://doi.org/10.1016/j.proeng.2017.04.045).

- 1292 Wang, G., Li, X., Liu, S., Gu, Y., 2018. Improved superplasticity and
1293 microstructural evolution of Ti2alnb alloy sheet during electrically as-
1294 sisted superplastic gas bulging. *Int J Adv Manuf Technol* doi:[10.1007/
1295 s00170-018-2431-x](https://doi.org/10.1007/s00170-018-2431-x).
- 1296 Wang, Z.j., Liu, J.g., Li, Y., 2010. Fracture prediction in non-isothermal
1297 viscous pressure bulging of aluminum alloy sheet using ductile fracture
1298 criterion. *Journal of Central South University of Technology* 17, 449–453.
1299 doi:[10.1007/s11771-010-0505-5](https://doi.org/10.1007/s11771-010-0505-5).
- 1300 Wu, Y., Liu, G., Liu, Z., Wang, B., 2016. Formability and microstructure of
1301 Ti22Al24.5Nb0.5Mo rolled sheet within hot gas bulging tests at constant
1302 equivalent strain rate. *Materials & Design* 108, 298–307. doi:[10.1016/j.
1303 matdes.2016.06.109](https://doi.org/10.1016/j.matdes.2016.06.109).